3-23-2017

RbHe Potential Energy Surface Sensitivity Study

Ethan D. Thorp

RBHE POTENTIAL ENERGY SURFACE SENSITIVITY STUDY

THESIS

Ethan D. Thorp, First Lieutenant, USAF

AFIT-ENP-MS-17-M-107

DEPARTMENT OF THE AIR FORCE
AIR UNIVERSITY

AIR FORCE INSTITUTE OF TECHNOLOGY

Wright-Patterson Air Force Base, Ohio

AFIT-ENP-MS-17-M-107

RBHE POTENTIAL ENERGY SURFACE SENSITIVITY STUDY

THESIS

Presented to the Faculty

Department of Engineering Physics

Graduate School of Engineering and Management

Air Force Institute of Technology

Air University

Air Education and Training Command

In Partial Fulfillment of the Requirements for the

Degree of Master of Science in Applied Physics

Ethan D. Thorp, BS

First Lieutenant, USAF

March 2017

AFIT-ENP-MS-17-M-107

RbHe Potential Energy Surface Sensitivity Study

Ethan D. Thorp, BS
First Lieutenant, USAF

Committee Membership:

Maj Charlton D. Lewis, Ph.D
Chair

Dr. David Weeks
Member

AFIT-ENP-MS-17-M107

Abstract

Many body quantum mechanics codes are used to calculate potential energy surfaces for interactions between atoms, surfaces calculated for Rubiduim-Helium interactions in a diode pumped alkali laser (DPAL) system are used. This paper studies how alterations of features on these surfaces effect the collisional cross section. The Split-Operator Method is used to propagate a wave function along the surfaces. Because the potential energy surfaces (PES) are coupled, the wave function can be transmitted from the starting surface to other energy levels. This transmittance is encoded in the correlation function. A split operator method is used to propagate the wave function under the full Hamiltonian, which is made of the electronic potential, the nuclear kinetic energy, and the Coriolis coupling. A Fourier transform is used to change from the position to momentum basis. In order to ensure the Hamiltonian matrix remains diagonal, adiabatic and diabatic matrices are calculated. The matrices are unitary and result in a diagonal Hamiltonian for the split operator method. The correlation function is used to to generate the Scattering Matrix elements. These elements describe the transmittance and reflectance of the reactant wave packet, as well as the phase shift from the interaction with the potential. A temperature averaged cross section is calculated using a theoretic collisional cross section from the $\Pi_{1/2}$ to the $\Pi_{3/2}$ states. Despite large changes in the correlation function and S-matrix elements, the temperature averaged cross section varied little and fell within the experimental error margins.

Table of Contents

List of Figures

Figure Page

RBHE POTENTIAL ENERGY SURFACE SENSITIVITY STUDY

I. Introduction

In order to maintain it's status as the most technologically advanced air force in the world, the United States Air Force has a vested interest in developing next generation weapons to maintain superiority in air, space, and cyber-space. Because of this drive, high energy lasers (HEL) are a priority to the Air Force. HEL provide many strategic advantages in areas such as nuclear ICBM strike defense, base defense, and carrier defense. Offensive capabilities are also options for air-borne platforms, in particular as a counter to unmanned aerial vehicles (UAV). In the space domain HEL provide a large advantage over conventional munitions to clear debris and potentially protect on orbit assets. Unlike conventional munitions, lasers leave no debris which could collide with satellites and can be used to break apart debris currently in orbit and push it into atmosphere to be burnt up. A leading candidate system for HEL systems is the Diode Pumped Alkali Laser (DPAL).

The DPAL system uses collisions of alkali metal atoms with noble gas atoms to de-excite electrons in the $^2P_{3/2}$ electronic states of the metal atoms that have been optically pumped from the ground, $^2S_{1/2}$.[28, 11, 23, 17, 3, 24, 7] The buffer gas collisionally de-excites the $^2P_{3/2}$ electrons to the $^2P_{1/2}$ energy level. These collisions happen fast enough to create a population inversion between the $^2P_{1/2}$ and $^2S_{1/2}$ levels, permitting lasing between the two levels to occur. Figure 1 shows the path through which electrons are excited, de-excited, and lased through the energy levels of the alkali metal.[28, 11, 23, 17, 3, 24, 7] The description of the DPAL system utilize statistical mechanics to describe the ensemble of metal and gas atoms, the Block

Born-Oppenheimer approximation to separate the nuclear and electronic dynamics of a singular collision, and many-body quantum mechanics theory to determine potential energy surfaces that describe the energy levels of the metal-gas system. This paper focuses on the interaction between rubidium and helium atoms, using previously calculated PES utilizing Many-body[5] theory. The large mass difference between the nuclei and electrons permits the use of the Born-Oppenheimer approximation, meaning the wave function can be separated into nuclear and electronic component wave functions such that $\Psi_{Total} = \Psi_{Electron} \times \Psi_{Nuclear}$. This allows the relative motion of the electrons to be ignored as the nuclei move closer, creating a PES only dependent on the distance between the nuclei rather than accounting for the the positions of all charged particles in the Coulomb potential.

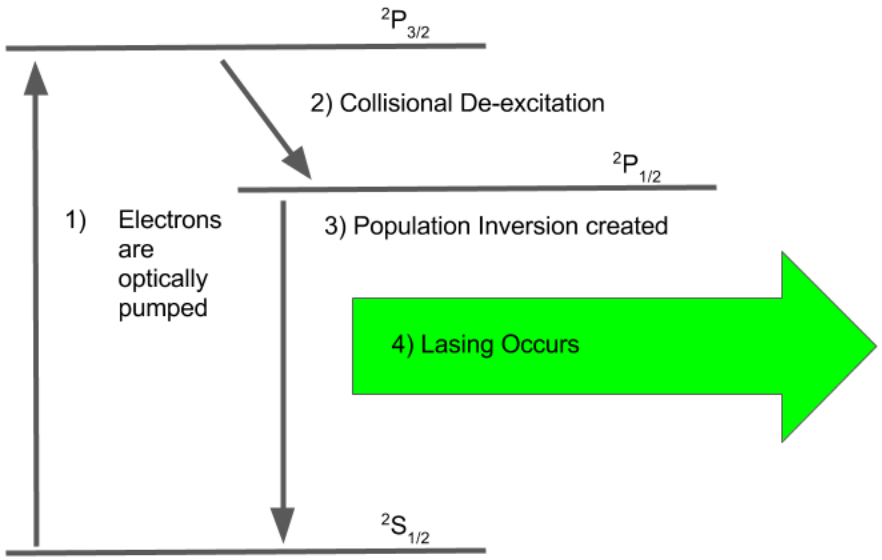

Figure 1. Energy level diagram for lasing in a DPAL system. Electrons are optically pumped from the $^2S_{1/2}$ state to the $^2P_{3/2}$. These electrons are the de-excited to the $^2P_{1/2}$ by colliding with a buffer gas, once a population inversion is created between the $^2P_{1/2}$ and $^2S_{1/2}$ states the system lases.

In order for quantum mechanical simulation of the DPAL processes to be successful, we require potential energy surfaces that have been calculated with enough accuracy that the resulting calculations reasonably agree with experiment.[12, 16, 15, 8, 6, 4] In particular this paper is concerned with how minor changes in the PES effect the collisional cross section to determine which features these parameters are sensitive to. The calculation of the initial PES requires large computational resources for the accuracy needed to model the DPAL system. By finding the sensitivity of the PES to minor changes in the features of the surface can help future calculations maximize accuracy while reducing computation time by avoiding over calculating features that have little impact on line broadening and shifting.

Time dependent propagation is used to calculate the scattering $\hat{S}$-matrix for RbHe surfaces. The calculations are done using an Anaconda Python distribution to leverage the computational efficiencies provided by graphical processing units (GPU). This increased efficiency allows for wave packet propagation on many surfaces quickly. Each calculation requires multiple runs, as the $\hat{S}$-matrix elements are parametrized by angular momentum, J, which ranges from $J = 0.5$ to $J = 250.5$, which allows for maximum utilization of the computational energy grid. Small changes are made to features of the surfaces and the calculation is redone for each value of J. Changes in the collisional cross section are used to determine the level of sensitivity in the potential energy surfaces and by extension what relative accuracy is needed in the initial potential energy surface calculations to match experimental error measurements.

II. Theory

2.1 Hamiltonian

The potential is generated by starting with computational surfaces calculated by Blank[5] using many body quantum mechanics code for the interaction of Rubidium (Rb) and Helium (He) atoms. The Born-Oppenheimer approximation is used so that the movement associated with the nucleus of each atom may be ignored. The Blank surfaces are used to generate a larger grid for the necessary potentials as well as the corresponding grid for the separation between the two nuclei (rGrid).[5, 7] This is done using a linear interpolation that is then padded on the end to make the number of grid elements a power of 2, this is done to fully optimize the needed Fast Fourier Transform (FFT) algorithms. These calculations were done using the first four calculated surfaces: $X\Sigma$, $A\Sigma$, $A\Pi_{\frac{1}{2}}$, and $A\Pi_{\frac{3}{2}}$, are shown in Figs. 2 and 3. The Blank surfaces combined with the spin-orbit coupling make up the electronic Hamiltonian in the adiabatic representation.[5, 7] In addition to the electronic and kinetic portions of the Hamiltonian, there is Coriolis coupling that plays a large role for higher total angular momentum, J. The full Hamiltonian is the sum of these individual parts.

$$\hat{H} = \hat{H}_{elec} + \hat{H}_{AngularKineticEnergy} + \hat{H}_{radial} \tag{1}$$

where

$$\hat{H}_{Elec} = \hat{H}^0_{RbHe} + \hat{H}_{so} \tag{2}$$

$$\hat{H}_{AngularKineticEnergy} = \frac{\hat{L}^2}{2\mu\hat{R}^2} \tag{3}$$

$$\hat{H}_{Radial} = \frac{\hat{P}^2_R}{2\mu} \tag{4}$$

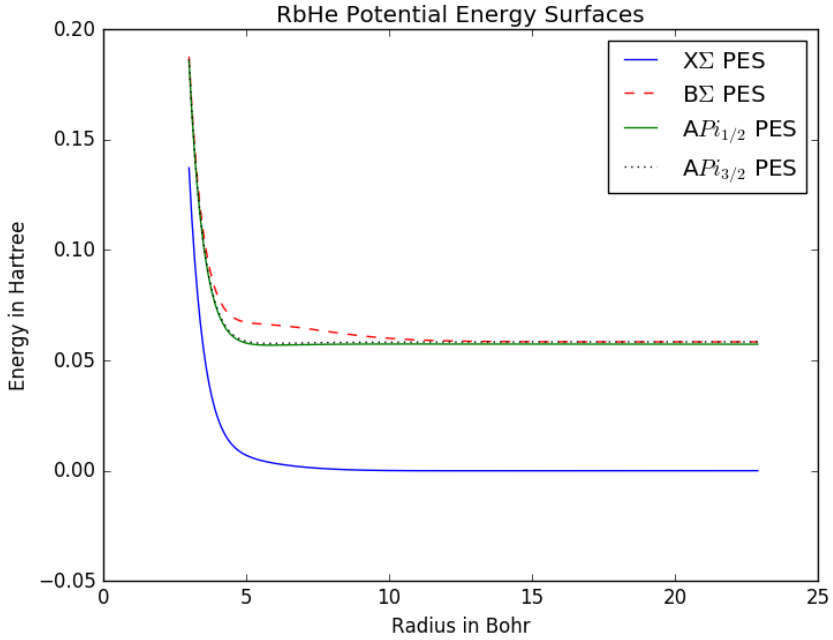

Figure 2. PES for RbHe system. The lowest surface is the ground state of the RbHe system. The lasing process takes place with the Rb in an already excited state, with electrons being promoted from the $A\Pi_{1/2}$ to the $B\Sigma_{1/2}$ surface.

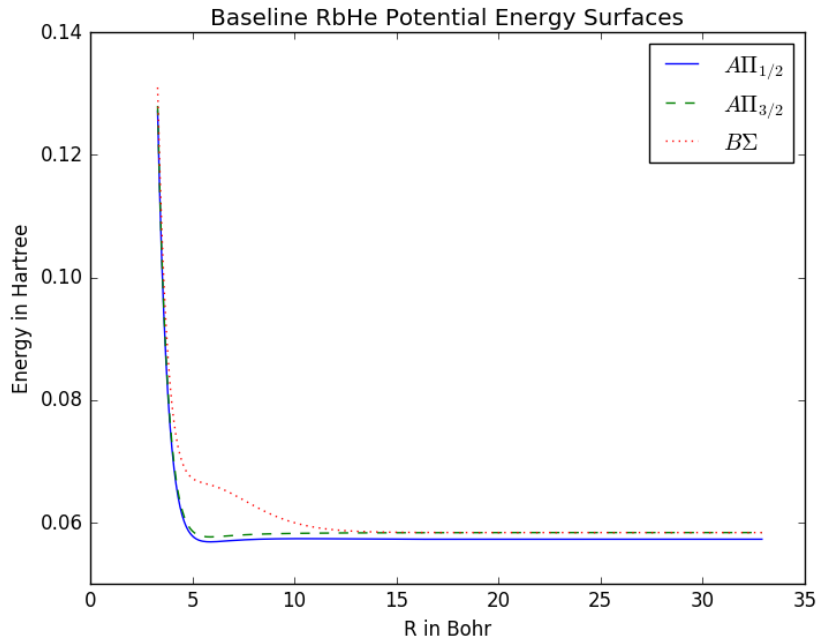

Figure 3. Lasing Surfaces for RbHe system. These are the spin orbit coupled surfaces on which the wave packet propagates.

The electronic Hamiltonian in the adiabatic representation is already diagonal. In order to calculate the adiabatic to diabatic transform matrix and it's inverse the potential needs to be undiagonalized, i.e. the diabatic representation[7]. The electronic diabatic matrix is given as,

$$\mathbb{V}_{elec} = \begin{pmatrix} \Pi + \frac{a(R)}{2} & 0 & 0 & 0 & 0 & 0 \\ 0 & \frac{2\Sigma+\Pi}{3} + \frac{a(R)}{2} & \mp\frac{\sqrt{2}}{3}(\Sigma+\Pi) & 0 & 0 & 0 \\ 0 & \mp\frac{\sqrt{2}}{3}(\Sigma+\Pi) & \frac{(\Sigma+2\Pi)}{3} - a(R) & 0 & 0 & 0 \\ 0 & 0 & 0 & \Pi + \frac{a(R)}{2} & 0 & 0 \\ 0 & 0 & 0 & 0 & \frac{2\Sigma+\Pi}{3} + \frac{a(R)}{2} & \mp\frac{\sqrt{2}}{3}(\Sigma+\Pi) \\ 0 & 0 & 0 & 0 & \mp\frac{\sqrt{2}}{3}(\Sigma+\Pi) & \frac{(\Sigma+2\Pi)}{3} - a(R) \end{pmatrix} \tag{5}$$

with,

$$\Sigma = \frac{1}{3}(2\Pi 1/2 - \Pi_{3/2} + 2\Sigma_{1/2} + \sqrt{(\Pi_{1/2})^2 + 2\Pi_{1/2}\Pi_{3/2} - 2(\Pi_{3/2})^2 - 4\Pi_{1/2}\Sigma_{1/2} + 2\Pi_{3/2}\Sigma 1/2 + (\Sigma_{1/2})^2}) \tag{6}$$

$$\Pi = \frac{1}{6}(\Pi 1/2 + 4\Pi_{3/2} + \Sigma_{1/2} - \sqrt{(\Pi_{1/2})^2 + 2\Pi_{1/2}\Pi_{3/2} - 2(\Pi_{3/2})^2 - 4\Pi_{1/2}\Sigma_{1/2} + 2\Pi_{3/2}\Sigma 1/2 + (\Sigma_{1/2})^2}) \tag{7}$$

$$a = \frac{1}{3}(-\Pi 1/2 + 2\Pi_{3/2} - \Sigma_{1/2} + \sqrt{(\Pi_{1/2})^2 + 2\Pi_{1/2}\Pi_{3/2} - 2(\Pi_{3/2})^2 - 4\Pi_{1/2}\Sigma_{1/2} + 2\Pi_{3/2}\Sigma 1/2 + (\Sigma_{1/2})^2}) \tag{8}$$

$\mathbb{V}_{elec}$ can be derived by starting with six Hund's case (c) basis eigen-vectors.

$$\hat{R}\left|R, {}^{Jj}_{\Omega\omega}\right\rangle = R\left|R, {}^{Jj}_{\Omega\omega}\right\rangle \tag{9}$$

$$\hat{J}^2\left|R, {}^{Jj}_{\Omega\omega}\right\rangle = \hbar^2 J(J+1)\left|R, {}^{Jj}_{\Omega\omega}\right\rangle \tag{10}$$

$$\hat{j}^2\left|R, {}^{Jj}_{\Omega\omega}\right\rangle = \hbar^2 j(j+1)\left|R, {}^{Jj}_{\Omega\omega}\right\rangle \tag{11}$$

$$\hat{J}_{\bar{z}}\left|R, {}^{Jj}_{\Omega\omega}\right\rangle = \hbar\Omega\left|R, {}^{Jj}_{\Omega\omega}\right\rangle \tag{12}$$

$$\hat{j}_{\bar{z}} \left| R, {}^{J\,j}_{\Omega\omega} \right\rangle = \hbar\omega \left| R, {}^{J\,j}_{\Omega\omega} \right\rangle \tag{13}$$

Hund's case (c) is used to project the total angular momentum, J, onto the inter-nuclear axis using $\hat{\Omega}$. The total electronic angular momentum, $j = l + s$, and total angular momentum are restricted to 3/2 and 1/2 while the projection of the electronic angular momentum, ω, is limited to $\pm 1/2$ and $\pm 3/2$ for the spin up and spin down orientations; l is the electronic orbital angular momentum and s is the spin angular momentum. $J_{\bar{z}}$ and $j_{\bar{z}}$ are the projection of the total angular momentum and total electronic angular momentum on the z axis. From the uncoupled electronic Hamiltonian the full Hamiltonian is created by using the Clebsch-Gordan coefficients, resulting in[20, 1, 21, 7]:

$H^0_{RbHe} + H_{so} =$

$$\begin{pmatrix} \Pi + \frac{a(R)}{2} & 0 & 0 \\ 0 & \frac{(2\Sigma+\Pi)}{3} + \frac{a(R)}{2} & \mp\frac{2^{1/2}}{3}(\Sigma - \Pi) \\ 0 & \mp\frac{2^{1/2}}{3}(\Sigma - \Pi) & \frac{(\Sigma+2\Pi)}{3} - a(R) \end{pmatrix} \tag{14}$$

Then by setting equation (14) equal to the adiabatic representation equations (6), (7), and (8) can be solved. These surfaces are shown in Fig 4.[7] The coupling region is where momentum transfer from one surface to another is permitted. As total angular momentum is increased more energy is required to reach the coupling region and less transmission is possible.

The impact of total angular momentum, J, is recorded in the $\hat{H}_{AngularKineticEnergy}$ matrix. The matrix is derived from the nuclear angular momentum operator $\hat{L} = \hat{J} - \hat{j}$, where $\hat{j}$ is the electronic angular momentum. From Eqn (3) the Angular Momentum matrix is generated by expanding $\hat{L}^2$, as shown in Eqn (15).

$$\hat{L}^2 = \hat{J}^2 - 2\hat{J}\cdot\hat{j} + \hat{j}^2 \tag{15}$$

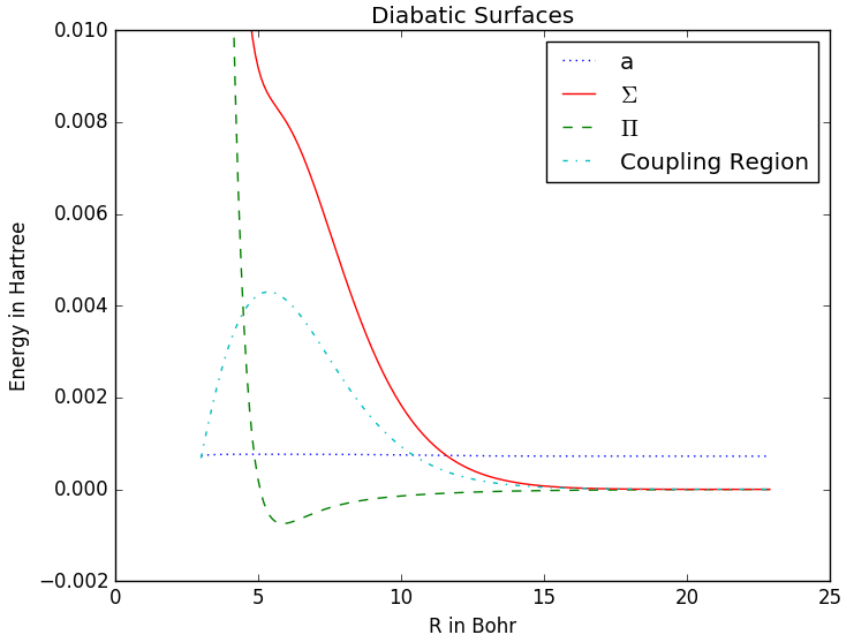

Figure 4. The Σ, Π, and a surfaces used to generate the diabatic potential are used to determine the coupling region. The coupling region is where transfers from one surface to another are permitted.

The Coriolis coupling matrix in the Hund's case (c) representation is given by,

$$\mathbb{V}_{Angular} =$$

$$\frac{\hbar}{2\mu R^2}\begin{pmatrix} J(J+1)-\frac{3}{4} & b & 0 & 0 & 0 & 0 \\ b & J(J+1)+\frac{13}{4} & 0 & 0 & 2(J+1) & 0 \\ 0 & 0 & J(J+1)+\frac{1}{4} & 0 & 0 & -(J+1) \\ 0 & 0 & 0 & J(J+1)-\frac{3}{4} & b & 0 \\ 0 & -2(J+1) & 0 & b & J(J+1)+\frac{13}{4} & 0 \\ 0 & 0 & -(J+1) & 0 & 0 & J(J+1)+\frac{1}{4} \end{pmatrix} \tag{16}$$

with,

$$b = -\sqrt{3(J-\frac{1}{2})(J+\frac{3}{2})} \tag{17}$$

2.2 Wave Packet Propagation

The collisional cross section relies on the scattering matrix elements. The S-matrix elements are calculated using the Channel Packet Method (CPM)[27, 26, 25, 9, 10, 19, 22] by calculating the overlap of the propagating reactant Möller state ($|\Psi_+\rangle$) with the stationary product ($|\Psi_-\rangle$) Möller states. This function of time called the correlation function. The reactant and product Möller states are the result of sending the initial wave packet to infinity in time and space and then returning to the initial position. The propagating reactant Möller state is the result of sending the reactant Möller state into the potential energy surface. Both of these are calculated using the time dependent Schrödinger equation: $i\hbar\frac{d}{dt}|\Psi\rangle = \hat{H}|\Psi\rangle$ with $\hat{H} = \frac{\hat{p}^2}{2m} + \hat{V}$. Due to the non-commutative nature of the $\hat{x}$ and $\hat{p}$ operators a Split Operator method is used to propagate the reactant Möller states such that:

$$e^{\frac{-it}{\hbar}\hat{H}} = e^{\frac{-it}{2\hbar}\hat{V}} e^{-it\frac{\hat{p}^2}{2\mu}} e^{\frac{-it}{2\hbar}\hat{V}} \tag{18}$$

Using this formulation allows us to use adiabatic and diabatic transformation matrices, ensuring the split operator is diagonal for each split in the propagator. Keeping the PES matrices diagional permits exponentiation and allows the separation of terms in Eqn (1). A Fourier transform is used to change between the coordinate and momentum basis. After the transform, the matrix needs to be diagonalized again. The diagonalization matrix is calculated by finding the eigen-vectors of the potential energy matrix in the diabatic basis. This gives a matrix to transform from the Diabatic to Adiabatic representation, $\hat{U}_{DAT}$. By taking advantage of the Hermitian nature of the potential the Adiabtic to Diabatic transform, $\hat{U_{ADT}}$ can be found by transposing

DAT so that $\hat{U}^{\dagger}_{DAT} = \hat{U}_{ADT}$. The a full time step of δt increment then becomes

$$|\Psi_+(t+\delta t)\rangle = e^{\frac{-i\delta t}{2\hbar}\hat{V}}\mathbb{U}_{DAT}\mathcal{F}^{-1}(e^{-i\delta t\frac{\hat{p}^2}{2\mu}}\mathcal{F}(\mathbb{U}_{ADT}e^{\frac{-i\delta t}{2\hbar}\hat{V}}|\Psi_+(t)\rangle)) \tag{19}$$

Using $\mathbb{V}_{eff} = \mathbb{V}_{elec} + \mathbb{V}_{angular}$ in the diabatic representation, the diagonalization of V_{eff} is calculated by finding the eigen-vectors at each R. The eigen-vectors are then used to build $\mathbb{U}_{DAT}$ by loading the eigen-vectors as column vectors. $\mathbb{U}_{ADT}$ is then found by taking the transpose of $\mathbb{U}_{DAT}$. With the nuclear angular coupling included, the new, diagonal matrix is called the dynamic adiabatic surfaces.

2.3 $\hat{S}$-Matrix Calculation

At each time step of the propagation the correlation of the propagating reactant Möller state with the product Möller state is calculated. This generates the time dependent correlation function, $C(t)$, that is used to calculate the elements of the $\hat{S}$ matrix.

$$C(t) = \langle\Psi_+|\, exp(-\frac{it}{\hbar}\hat{H})\,|\Psi_-\rangle \tag{20}$$

The correlation function is a measure of the overlap of the propogating reactant Möller state with the product Möller state at time t. The overlap is used to determine what fraction of the wave is reflected off the initial potential energy surface and what fraction is transmitted to an upper energy surface. Using the Fourier pair relationship between time and energy, a Fourier transform of the correlation function is made to compute $C(E)$. The C(E) function is then normalized using the momentum associated with the initial wave packets,

$$S_{\pm k'\pm k}(E) = \frac{\hbar^2(|k'||k|)^{1/2}}{(2\pi\mu)\eta^*_-(\pm k')\eta_+(\pm k)}\int_{-\infty}^{+\infty} e^{iEt}C(t)dt \tag{21}$$

Each element represents the amount of incoming wave that is reflected or transmitted from or to each surface at energy, E. For example, $S^2_{+k_1,-k_1}$ is the fraction of the incoming wave that is reflected back on the same surface, the reflection coefficient R. $S^2_{+k_2,-k_1}$ is the transmission coefficient from surface one to a second coupled surface. The S-matrix is unitary which means that $R_{k'k} + \sum_{k'} T_{k'k} = 1$.

2.4 Collisional Cross Section

Classically, chemical cross sections use a hard body approximation to determine the interaction cross section.[14] This approximation assumes a reaction takes place if the separation of particles is less than or equal to the radii of the two spheres, meaning the probability of transmission would be one for any reaction. This is clearly not the case for a quantum mechanical system and a measure of the probability of transmission is needed. The S-matrix elements squared give the probability of transmission, a successful reaction, and reflection, no reaction. Once the S-matrix elements are calculated they can be used to calculate collisional cross section for interactions between states using Eqn. 22.[7, 14] The sum need only be done to the point where the angular momentum potential stops the wave packet from reaching the coupling region of the electronic potential. For these calculations a J_{max} of 250.5 is used, determined from by the experimental convergence of the cross sections[12].

$$\sigma_{j',\omega' \leftarrow j,\omega}(E) = \frac{\pi}{k^2_{j',\omega'}} \sum_{J=0.5}^{\infty} (2J+1)|S^J_{j',\omega' \leftarrow j,\omega}(E)|^2 \tag{22}$$

The experimental measurements used for the comparison are from the ${}^2P_{3/2} \leftarrow {}^2 P_{3/2}$ transition. The expansion for this transition is worked out in 23.

$$\begin{aligned}
&\sigma_{^2P_{3/2}\leftarrow{}^2P_{1/2}}(E) = \\
&\sum_{\omega=-1/2}^{1/2} (1/2)[\sigma_{3/2,-3/2\leftarrow 1/2,\omega}(E) \\
&+ \sigma_{3/2,-1/2\leftarrow 1/2,\omega}(E) \\
&+ \sigma_{3/2,3/2\leftarrow 1/2,\omega}(E) + \sigma_{3/2,1/2\leftarrow 1/2,\omega}(E)].
\end{aligned} \tag{23}$$

Once the theoretic cross section is calculated it can be convolved with the Boltzman distribution, as in Eqn. 24, to provide a calculation that can be compared with experiment. This thermally averaged cross section is compared to the experimental measurements from Gallagher[12]. The temperature range from 0-400K contains two experimental measurements and sets the range for the calculation.

$$Q(T) = (k_B T)^{-2} \int_0^\infty E e^{-\frac{E}{k_B T}} \sigma(E) dE \tag{24}$$

III. Code Verification

3.1 One Dimensional Propagation

The first step is to create a working one dimensional propagation routine. The objective of this step is to test the approximation of the propagator against the analytic solution for transmission and reflection through a square well. Table 2 shows the initial conditions for the incoming wave packet used in Eqn. 26. The wave moves to the right, into the well where it scatters, as shown in Fig. 5.

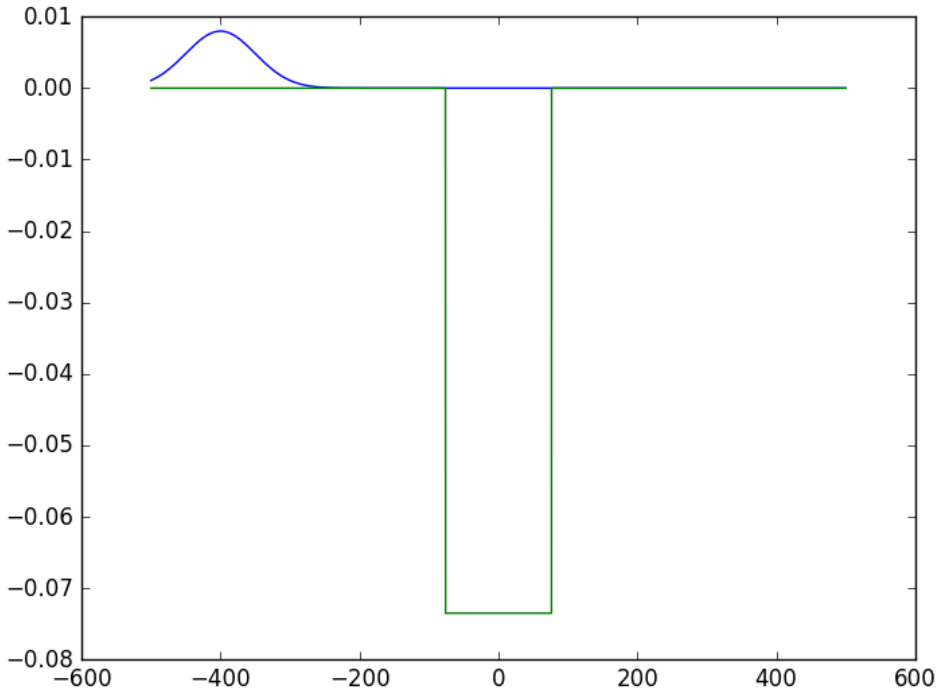

Figure 5. Starting Position of wave packet in relation to the square well. Energy is in Hartree on the vertical scale. The horizontal scale is in Bohr.

Part of the wave is transmitted and part is reflected. Absorbing boundary conditions, defined in Eqn. 27, are used simulate infinity and keep the wave from wrapping

around the grid. The boundary conditions are introduced by adding an imaginary part to the potential, and a Gaussian shape is used. The analytic solution is known for the square well reflection and transmission and is used to verify the code.[13] The inverse transmission coefficient is shown in Eqn 25. In Figure 6, the reflection and transmission coefficients are plotted together.

$$T^{-1} = 1 + \frac{V_0^2}{4E(E+V_0)} sin^2(\frac{2a}{\hbar}\sqrt{2m(E+V_0)}) \tag{25}$$

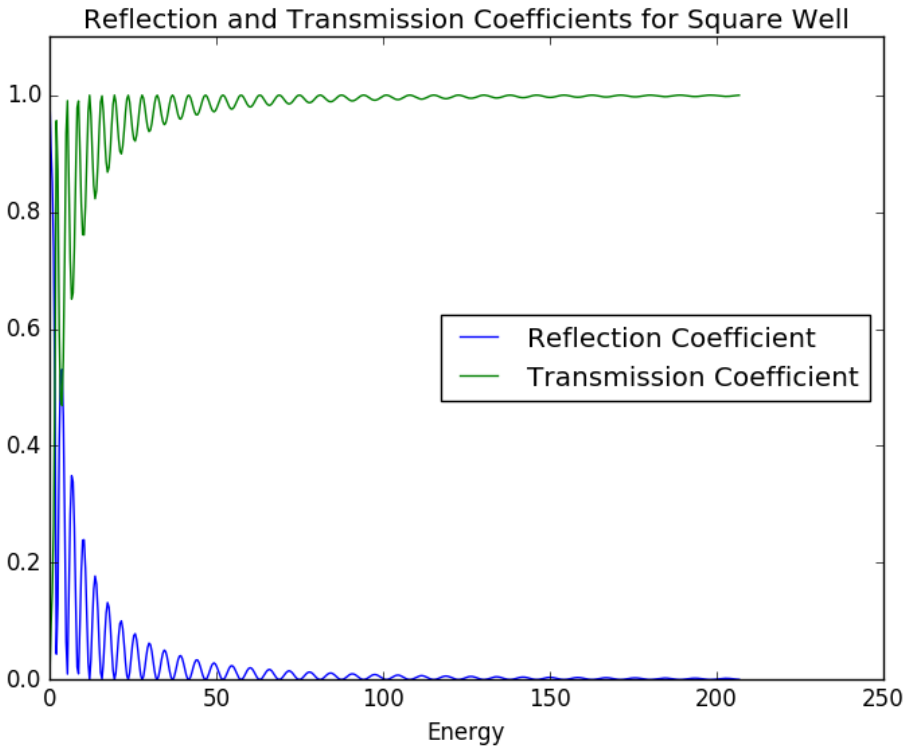

Figure 6. The reflection and transmission coefficients are plotted together to show how the oscillations line up as energies increase.

The oscillations line up with each other so that sum is of the two is always one, as shown in Figure 7. The osculations in Figure 7 for low energy are a result of errors in the split operator propagation.

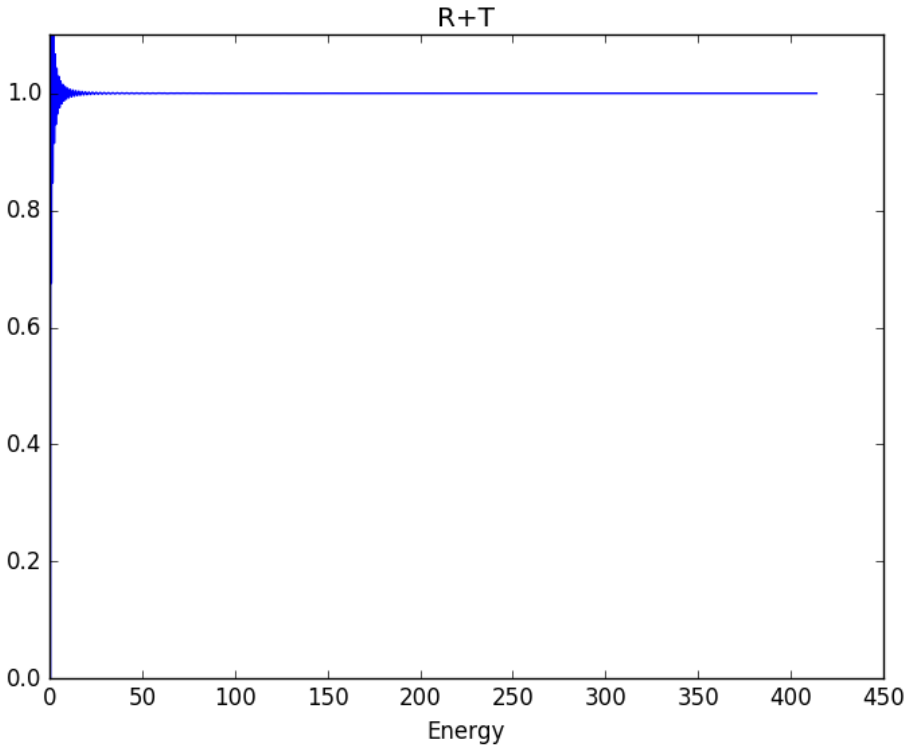

Figure 7. The sum of the reflection and transmission coefficients add to one as expected. Low energies see large oscillations where the content of the momentum packet is noisy.

The computed reflection coefficients are in strong agreement with the analytic shown in Fig 8

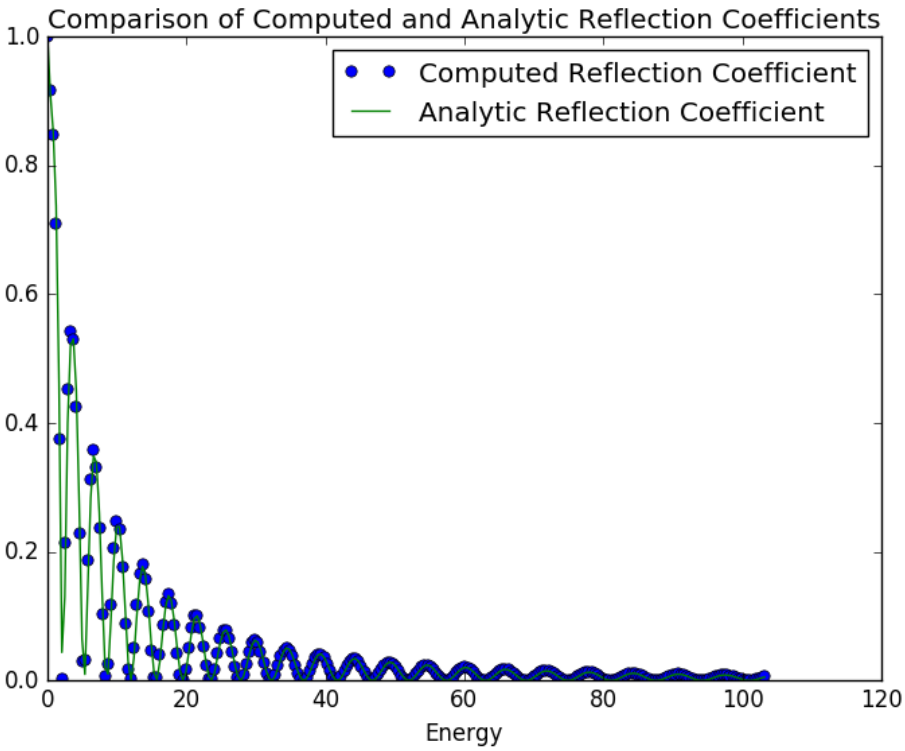

Figure 8. The solid green line is the analytic square well reflection. The dotted blue line is the computed square well reflection. There is strong agreement between the two.

$$\Psi = (\frac{2a}{\pi})^{1/4} \frac{1}{\sqrt{1+\frac{2ati}{m}}} exp(\frac{-a(x-x_0)^2 + ik_0(x-x_0) - \frac{itk_0^2}{2m}}{1+\frac{2ati}{m}}) \tag{26}$$

$$ABC = -0.5i\ e^{-0.001r^2} \tag{27}$$

Table 1. Parameters for square well propagation

Half Width	$50.a.u$	V_0	2 eV	x_{grid}	$\pm$500 a.u.
N	65536	dx	.0076	dk	.0076 a.u.
dt	1	Time Steps	10000		

Table 2. Wave Packet Parameters

Mass	5 a.u.	x_0	75 Bohr	k_0	3.0	a	2.0

3.2 Two Dimensional Propagation

Once the one dimension propagation was working, the next step is to create an algorithm for a two dimensional propagation that allows for coupling between the two states. The two state problem is used to generalize for N-state propagation. This step adds the need for the adiabatic and diabatic transform matrices in conjunction with the Fourier transform to propagate. A Gaussian is placed in one component of a two dimensional vector similar to the 1-D propagation for the incoming wave. This propagation is done under only a pseudo-electronic potential prepared by taking the Π, a, and Σ calculated from the Blank surfaces to form a diabatic potential, as in Eqn 28.

$$\mathbb{V}(R) = \begin{pmatrix} \Pi & a(R) \\ a(R) & \Sigma \end{pmatrix} \tag{28}$$

This creates a coupling between the two states and allowed transmission to the upper state. Due to the fact that there is no Coriolis coupling the initial placement of the wave function can be used rather than propagating to infinity and returning as is done in the calculation of the Möller states. Fig 9 shows the reflection and transmission S-matrix elements for this propagation. The red line shows that the S-matrix elements squared add to one for all energies, as expected.

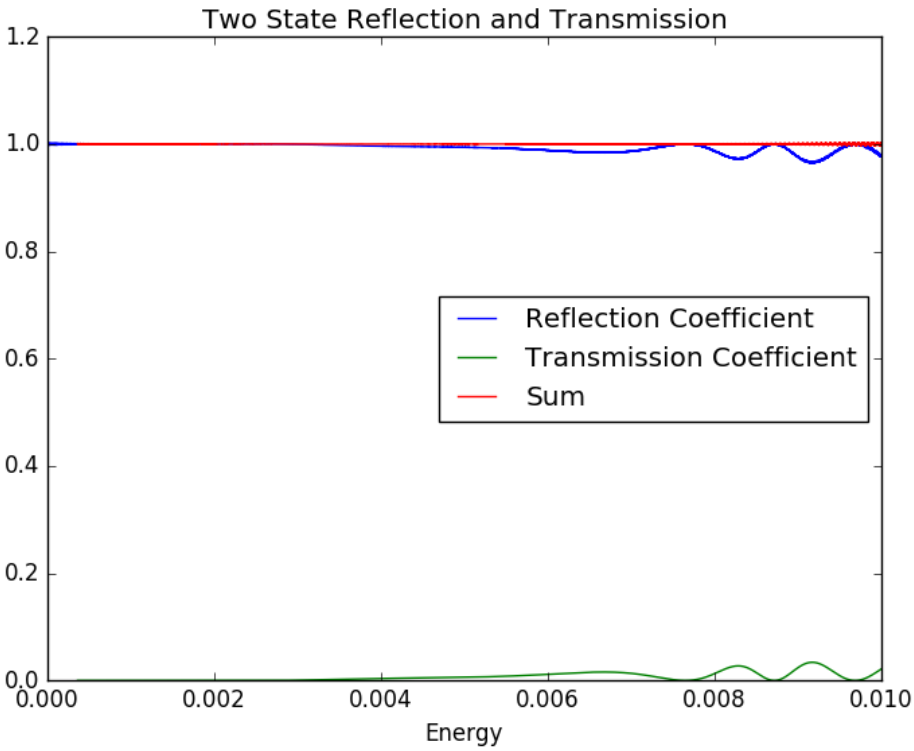

Figure 9. Two state reflection and transmission coefficients are plotted against energy. The red line shows that the elements add to one as expected.

IV. Computation

Computation was attempted at first with the full six dimension Hamiltonian and the ground state, created in a seven dimensional matrix. Due to an unknown error in the code, correlation functions for the modified surfaces did not converge to the baseline for high J as expected. This lead to a transition from the GPU processing to a three dimensional approximation on the CPU using legacy code.

4.1 Computer Specifications

This project used an Anaconda Python distribution from Continuum Analytics as the base programming language. This distribution came with libraries designed to utilize GPUs, libraries written specifically written for NVIDIA graphics cards. The computer used was equipped with a NVIDIA Quadro M4000 graphics card that was used for display, a NVIDIA Tesla K80 for the matrix multiplication needed for wave packet propagation, and 16 physical CPU cores, used for the calculation of the S-matrix elements, collisional cross section, and operating system calls. The K80 has 4992 cores and 24 gigabytes of random access memory allowing large grids to be stored and processed simultaneously. The python libraries "numba" and "accelerate" comes with two sub-libraries, "vectorize" and "guvectoize" , that are used to import the GPU command scripts. For arrays stored on the GPU, "vectorize" replaces for loops that are independent of the previous iteration. The call to "guvectorize" is an optimized version of "vectorize" designed to iterate over matrices rather than the vector only inputs of "vectorize". The legacy code that was later used was Fortran 90 and was distriubted across multiple computers and CPUs.

4.2 7-Dimensional Calculation

The calculations were first attempted using a 7-dimensional array that includes the ground level S-manifold, necessary for calculations of line broadening and shifting, with equations (5) and (16) describing the P-manifold. In the diabatic representation the potential used for computation is,

$$V(R) = \begin{pmatrix} XSigma & 0 & \cdots & 0 \\ 0 & V_{eff} & \cdots & \cdots \\ \vdots & \vdots & \ddots & \\ 0 & \vdots & & \ddots \end{pmatrix} \tag{29}$$

This is done for computational efficiency, to fully utilize the GPUs. The ground state reflection and transmission can be done separately if desired or resources allowed. The zeroes used to fill in the rest of the matrix ensure that there is no coupling between the ground state and the lasing surfaces. This potential is then used to calculate the $\mathbb{U}_{DAT}(R)$ and $\mathbb{U}_{ADT}(R)$ matrices. These were then checked to ensure that $\mathbb{U}_{DAT}(R)\mathbb{U}_{ADT}(R) = \mathbb{I}(R)$. The momentum grid (kgrid) that is used for propagation in momentum space is created using Fourier Theory. To find the maximum grid momentum use the grid spacing, dr, and the relationship $dr * k_{max} = \pi$. This grid is swapped so that the zero element is first followed by the positive values then followed by the negative values. This optimizes the chain of Fourier transforms by matching the output order of the forward FFT. The reactant Möller states were pre-calculated by placing a Gaussian at 100 Bohr on the rGrid and propagating to infinity then back to 100 Bohr under the centrifugal potential for each value of J.

The propagation starts at $t = 0$ and progresses by $dt = 20$ in atomic units (A.U.). For each time step the wave packet moves through the potential by looping over every point on the rGrid. After the wave is calculated at each value of r, it is transformed

from the adiabatic representation to the diabatic representation. This is then transformed into the momentum representation. The wave packet is then multiplied by the exponential of momentum squared for each value in kGrid by looping over the length of the swapped grid. After each value of k has been evaluated the wave packet is transformed back to the r basis, and then to the adiabatic representation. The second half of the split operator potential the acts on the wave packet, completing the split-operator calculation. Finally, the correlation function is calculated using Eq 20. Time is incremented by dt and the loop repeats until the wave has completely left the potential at total propagation time, T. At the end of the loop a complete correlation function, $C(t)$, is output with $\frac{T}{dt}$ entries. In order for accurate $\hat{S}$ matrix elements it is important to ensure all of the wave exits the potential, this is determined empirically by noting when the transmission and reflection coefficients sum to one across all energies. Computational artifacts make the edges of the energy grid an exception to this. The correlation function is the main computational hurdle and is handled exclusively on the GPUs. The correlation function is the result of the main algorithm and is responsible for consuming most of the computational resources. After the wave propagation is complete, the correlation function is passed to the CPUs for the final calculation of the S-matrix elements. The 7 dimensional calculation had to be abandoned do to an unidentified bug in the code that caused the sum of the S-matrix elements to grow beyond one, meaning the wave packet was gaining energy from its interaction with the potential. Fig 10 demonstrates the accumulation of energy from the potential. The blue curve is the reflection coefficient and the green curve the transmission coefficient.

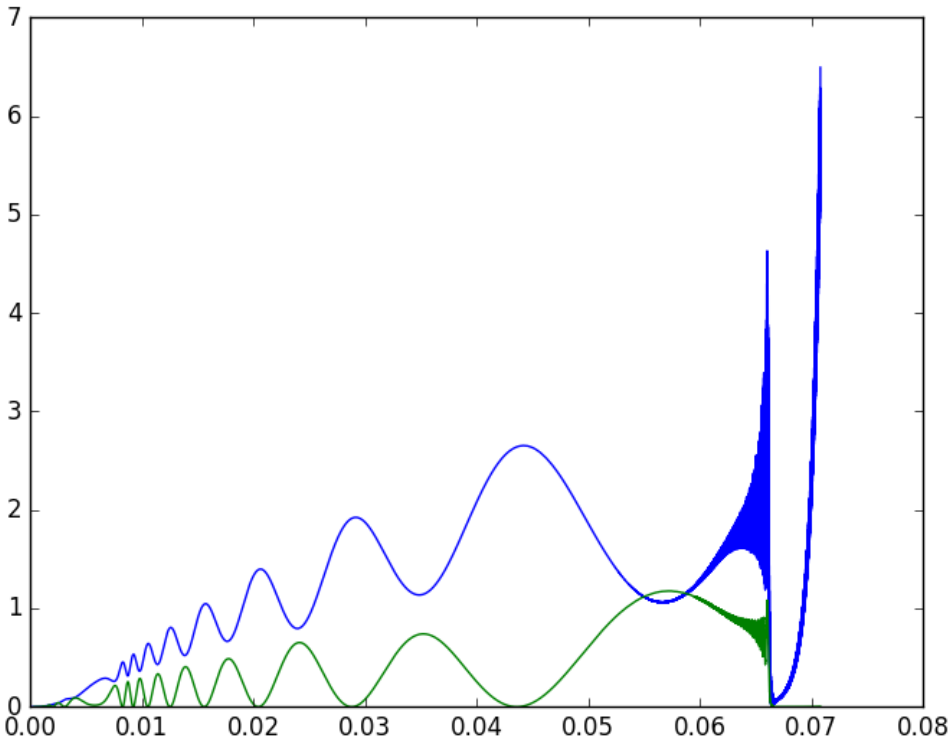

Figure 10. The blue curve is the reflection coefficient for the 7 dimension propagation for J=0.5. The green curve is the transmission coefficient. Both grow beyond one meaning that something unphysical is happening in the code.

4.3 3 Dimensional Approximate Propagation

After attempts to rectify the bug in the 7 dimensional failed, a fallback was carried out to use a 3 dimension propagation. This uses the electronic potential from Eqn 14 and the upper 3 dimension block from the angular momentum Hamiltonian, 30.

$$\mathbb{V}_{Angular} = \frac{\hbar}{2\mu R^2} \begin{pmatrix} J(J+1) - \frac{3}{4} & -\sqrt{3(J-\frac{1}{2})(J+\frac{3}{2})} & 0 \\ -\sqrt{3(J-\frac{1}{2})(J+\frac{3}{2})} & J(J+1) + \frac{13}{4} & 0 \\ 0 & 0 & J(J+1) + \frac{1}{4} \end{pmatrix} \tag{30}$$

Using the three dimension approximation forgoes the coupling from the angular momentum between the spin up and spin down orientations. For the cross section calculations, the symmetry between the spin up and spin down orientations allows one calculation to be run and then the result doubled to account for both. The three dimensional algorithm is the same as seven dimension propagation with the potential replaced. The Möller states were generated by propagating on this three dimensional matrix and are shown in Fig 11 for select J. Fortran 90 code was used for the propagation.

4.4 Modification of Potential

The purpose of this study is to measure the sensitivity of collisional cross section to changes in the potential energy surfaces with goal of informing future surface calculations. First, a baseline needs to be established by calculating the cross section of the original Blank surfaces. Two features on the surfaces were modified independently and then the Σ, Π, and a coefficients from Eq. $6, 7, 8$ were calculated. The features were:

- The shoulder on the B Σ surface located around 6 Bohr
- The height of the A $\Pi_{1/2}$ barrier at 10 Bohr

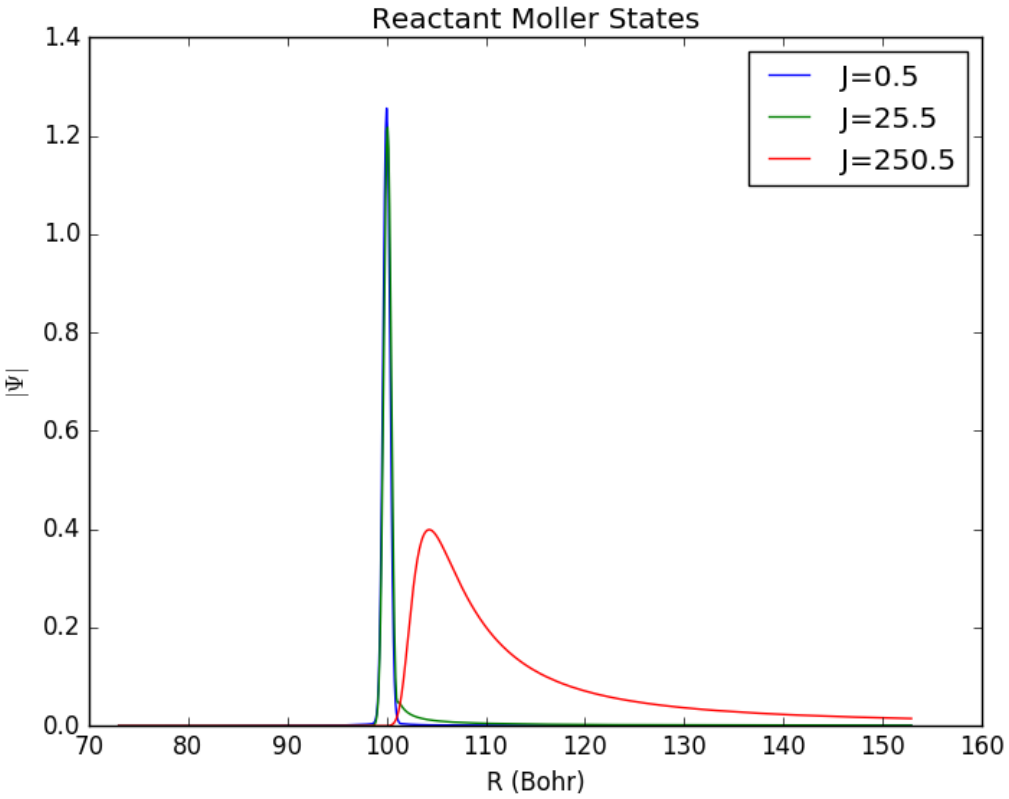

Figure 11. Reactant Möller states for J=0.5, 25.5, and 250.5. The states are stretched from the initial Gaussian shape and a tail is created for higher J when the initial wave propagates back from infinity under the angular potential.

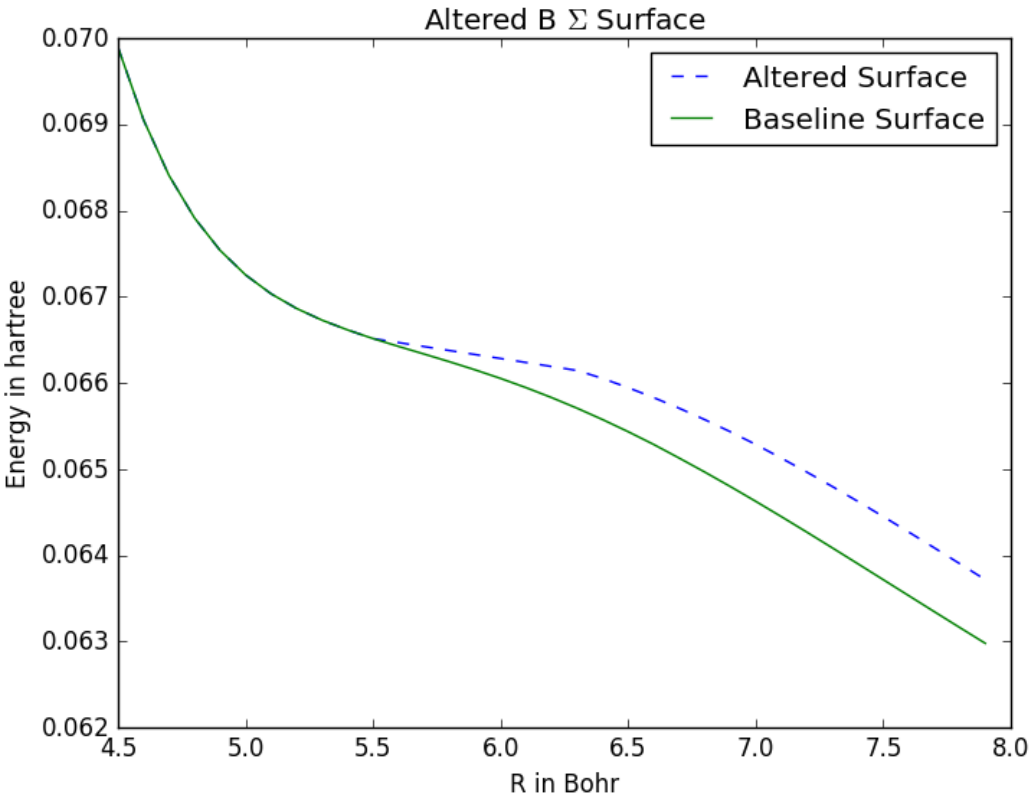

Figure 12. The location of $B\Sigma$ PES shoulder is extended to the right by 0.5 Bohr to test the impact of the location on the collisional cross section.

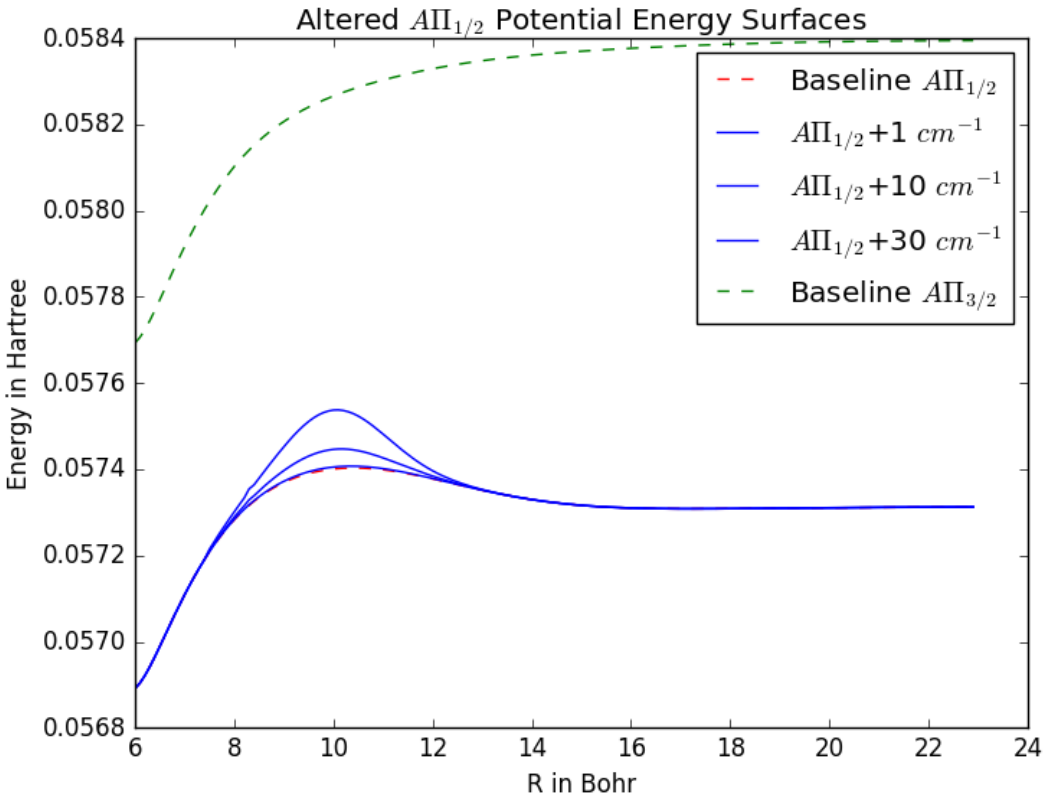

Figure 13. The barrier at the top of the well on the $A\Pi_{1/2}$ surface is increased by 1, 10, and 30 cm^{-1} to determine sensitivity of the line broadening and shifting coefficients to changes in the barrier height. The heights were chosen so that surfaces did not cross, insuring the modification did not violate the adiabaticity.

The shoulder on the $B\Sigma$ surface was modified by extending it to the right by a half Bohr, as shown in Fig. 12. Figure 13 shows the height of the modified PES. The upper surface is the $A\Pi_{3/2}$ surface, showing that the modification did not violate the adiabatic nature of the curves by crossing. The height of the barrier on the $A\Pi_{1/2}$ surface was raised by 1,10,and 30 wavenumbers which corresponds to .46%, 4.6%, and 13.8% of the energy difference of the asymptotic limits of the $\Pi_{3/2}$ and $\Pi_{1/2}$ surfaces. The energy gap is tied to the spin orbit splitting measured by experiment; Blank used the experimental values to set the asymptotic limit of his calculations.[5]

Modifying the surfaces also changes the coupling regions. There is little change to the coupling region for the alterations to the $\Pi_{1/2}$ surface but the alteration of the $\Sigma_{1/2}$ extends the coupling region, shown in Fig 14. This allows for a greater chance for the incoming wave to couple to a higher state as there is more time spent in the coupling region.

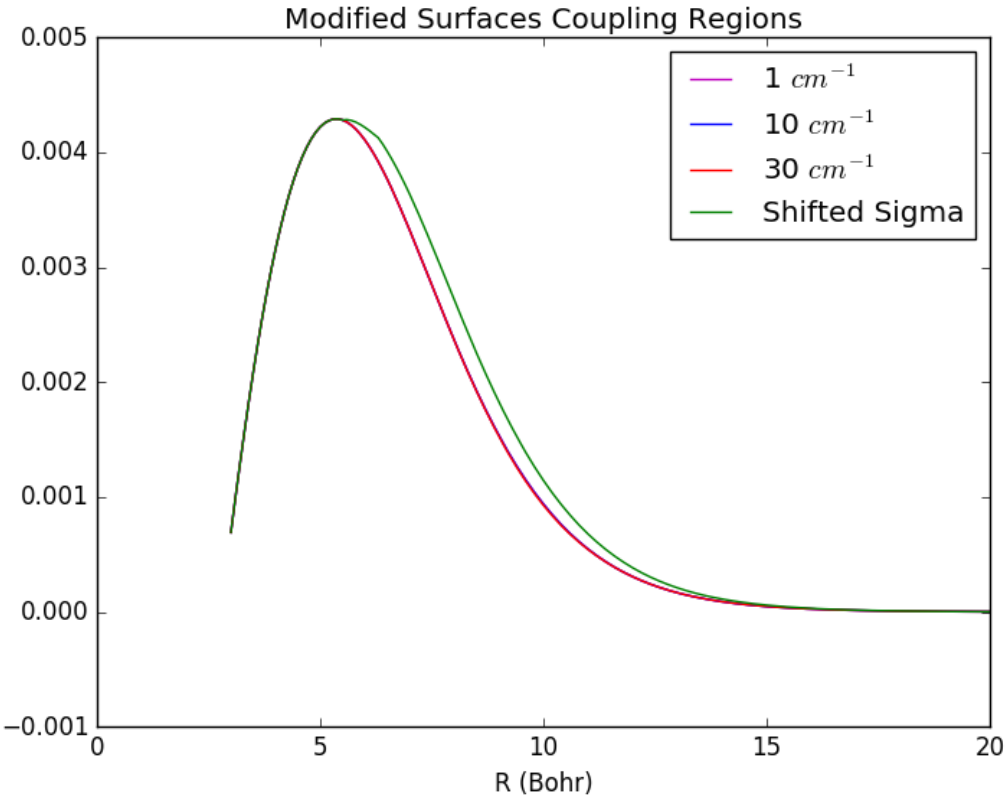

Figure 14. The coupling region has small change do to the alterations on the $\Pi_{1/2}$ surface, however, the changes to the $\Sigma_{1/2}$ surface extend the coupling region.

V. Results

Once the propagation was completed analysis of the results was done using CPU algorithms. This section explains the methods of analysis and the results. These include analysis of the correlation function, S-matrix elements, and cross sections. The temperature averaged cross sections are compared to experimental results.

5.1 Correlation Function Analysis

The first check on the change the modifications had was to compare the correlation functions of the baseline surfaces to those of the modified surfaces. Fig 15 shows the baseline correlation function on the left and the 1 cm^{-1} altered $\Pi_{1/2}$ correlation function for J=0.5. The top plots are the $\Pi_{1/2}$ to $\Pi_{1/2}$ correlation functions, then working down the $\Pi_{1/2}$ to $\Pi_{3/2}$, and finally the $\Pi_{1/2}$ to $\Sigma_{1/2}$. The small alteration had little effect on the correlation function and the wave packet spent close to the same amount of time in the well. The only noticeable change is a small extension of the plateau in the middle plot. A positive sign is that the small change did not create any transmission to $\Sigma_{1/2}$.

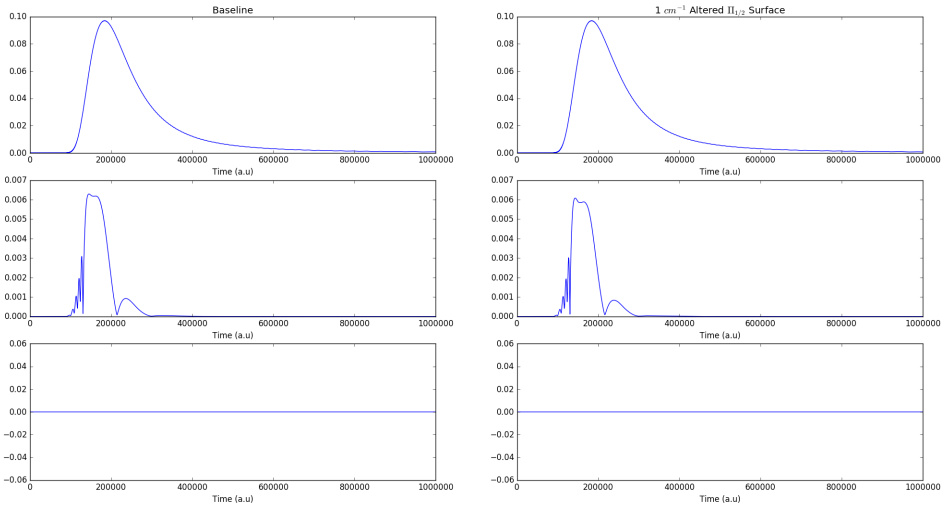

Figure 15. Correlation functions at J=0.5 for both the baseline and $1cm^{-1}$ altered surface are plotted against each other, with the top plots being the $\Pi_{1/2}$ to $\Pi_{1/2}$ correlation functions, then working down the $\Pi_{1/2}$ to $\Pi_{3/2}$, and finally the $\Pi_{1/2}$ to $\Sigma_{1/2}$.

The 30 cm^{-1} and shifted Σ surface had a larger impact on the correlation function. Fig 16 shows the 30 cm^{-1} altered surface for J=0.5. It is clear that the correlation function in the middle plot is shifted to the left meaning that the wave packet spent less time interacting with the potential. The primary peak is also larger meaning that more of the wave is transmitted to a higher state a result of decreasing the energy gap between states. The only portions of the wave packet that are transmitted are those that have enough energy to reach the top of the increased barrier, which requires more energy to reach. This higher energy requirement means that the faster moving parts of the wave function are what is transmitted, forcing the correlation function to peak at lower t.

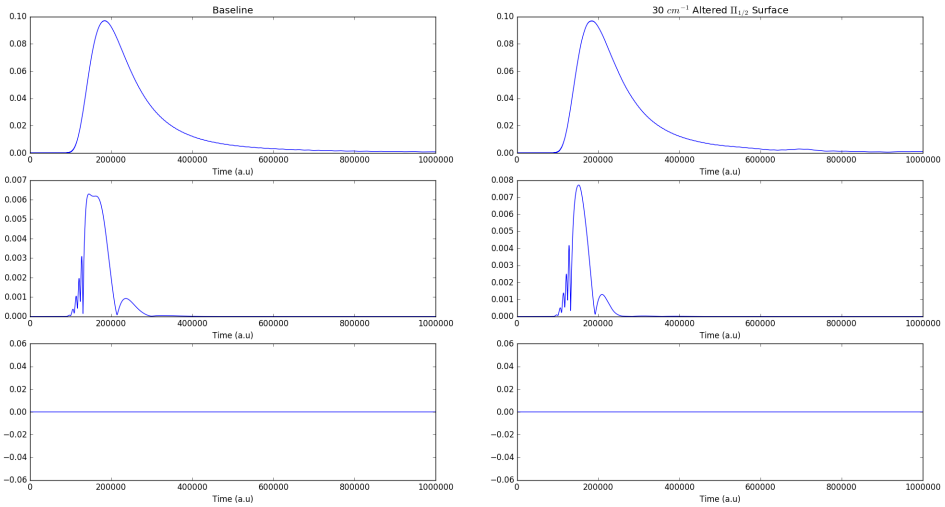

Figure 16. Correlation functions at J=0.5 for both the baseline and $30cm^{-1}$ altered surface are plotted against each other, with the top plots being the $\Pi_{1/2}$ to $\Pi_{1/2}$ correlation functions, then working down the $\Pi_{1/2}$ to $\Pi_{3/2}$, and finally the $\Pi_{1/2}$ to $\Sigma_{1/2}$.

In Fig 17, the shifted Σ correlation functions plotted with the baseline correlation functions at J=0.5. The change in the Σ surface lowered the overall transmission despite increasing the coupling region. The increased coupling region does allow slower moving parts of the wave packet to be transmitted as can seen in the longer duration of the correlation function in the middle right plot around t=300,000.

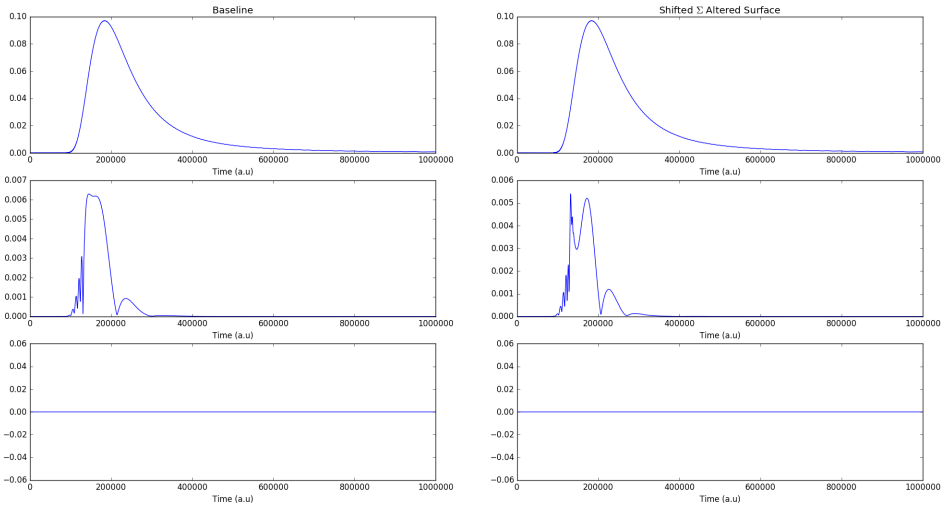

Figure 17. Correlation functions at J=0.5 for both the baseline and shifted Σ surface are plotted against each other, with the top plots being the $\Pi_{1/2}$ to $\Pi_{1/2}$ correlation functions, then working down the $\Pi_{1/2}$ to $\Pi_{3/2}$, and finally the $\Pi_{1/2}$ to $\Sigma_{1/2}$.

Increasing J to 25.5 allows transmission to the $\Sigma_{1/2}$ state. The largest changes were again seen in the 30 cm^{-1} and the shifted Σ surfaces. Small changes were also see in 10 cm^{-1} altered surface with no immediately noticeable changes in the 1 cm^{-1}. In Fig 18 the 30 cm^{-1} altered surface correlation functions are plotted. Changes in all three states are readily apparent in all three surfaces. There is greater transmission to the $\Pi_{3/2}$ state at earlier times. There is also less transmission to the $\Sigma_{1/2}$ surface. One of the more interesting features is the oscillations in the reflection shown in the top right plot. This may be caused by the increased barrier and the angular momentum potential forming a well that traps some of the wave packet which is slowly reflected out, creating a resonance.

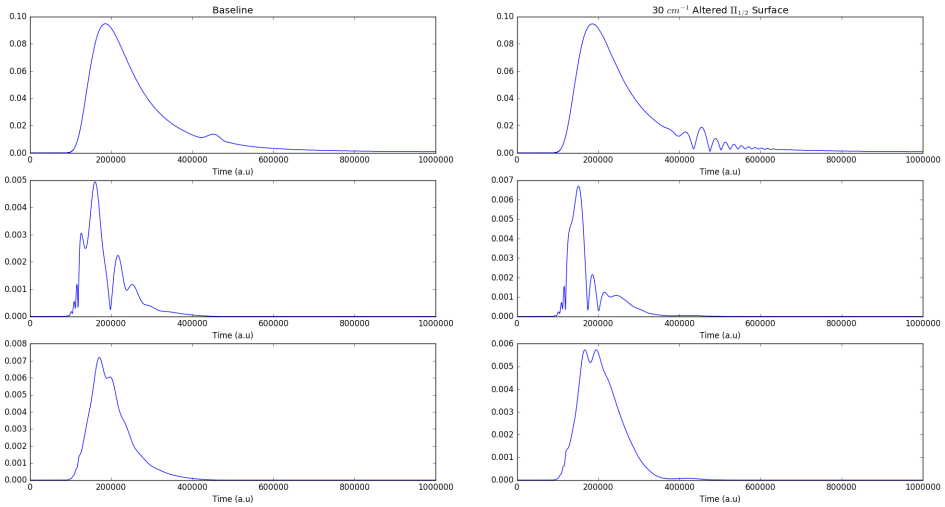

Figure 18. Correlation functions at J=25.5 for both the baseline and 30 cm^{-1} altered surface are plotted against each other, with the top plots being the $\Pi_{1/2}$ to $\Pi_{1/2}$ correlation functions, then working down the $\Pi_{1/2}$ to $\Pi_{3/2}$, and finally the $\Pi_{1/2}$ to $\Sigma_{1/2}$.

The shifted Σ alterations had little effect on the reflection or transmission to the $\Sigma_{1/2}$ state for J=25.5 but did change the transmissions to the $\Pi_{1/2}$ state significantly. The primary difference is the drop in early transmission to the $\Pi_{3/2}$. Later correlation is slightly greater in the modified surface and the entire correlation has happened earlier.

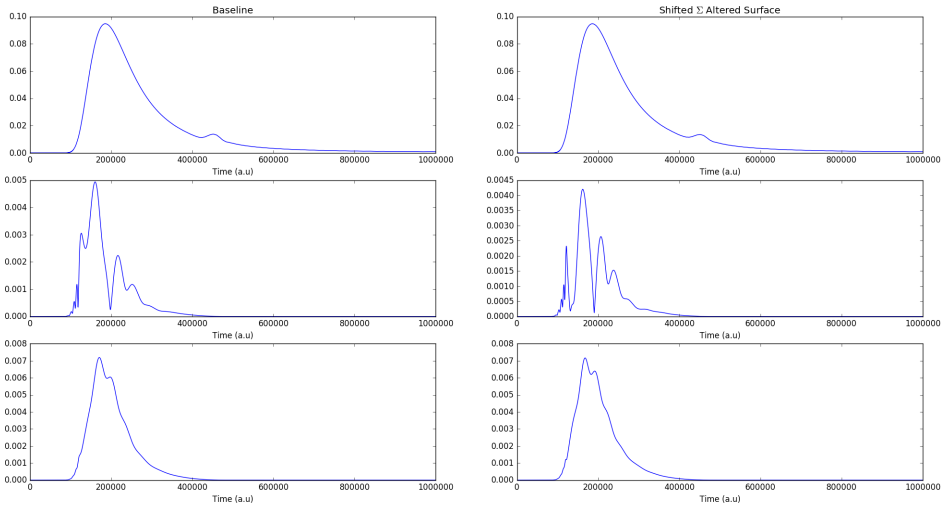

Figure 19. Correlation functions at J=25.5 for both the baseline and shifted Σ surface are plotted against each other, with the top plots being the $\Pi_{1/2}$ to $\Pi_{1/2}$ correlation functions, then working down the $\Pi_{1/2}$ to $\Pi_{3/2}$, and finally the $\Pi_{1/2}$ to $\Sigma_{1/2}$.

Another metric for the effect of the altered surfaces is the difference between the baseline correlation function and the modified correlation function. Eqn 31 is used to create a least squares measure for each value of J from 0.5 to 250.5.

$$\Delta = \int_0^T |C_{baseline}(t) - C_{Mod}(t)|dt \tag{31}$$

Figs 20, 22, 23, 24 show the difference between the baseline correlation function and the modified surfaces. As J increases, the the magnitude of the electronic potential becomes small compared to the centrifugal potential. This causes the difference to converge to zero for high J, as expected. The alterations to the $\Pi_{1/2}$ surface have minimal impact on the correlation functions for the $\Pi_{3/2}$ and $\Sigma_{1/2}$ surfaces. Fig 21 shows the $\Pi_{3/2}$ and $\Sigma_{1/2}$ displaying the same behavior of the $\Pi_{1/2}$ surface with a smaller magnitude.

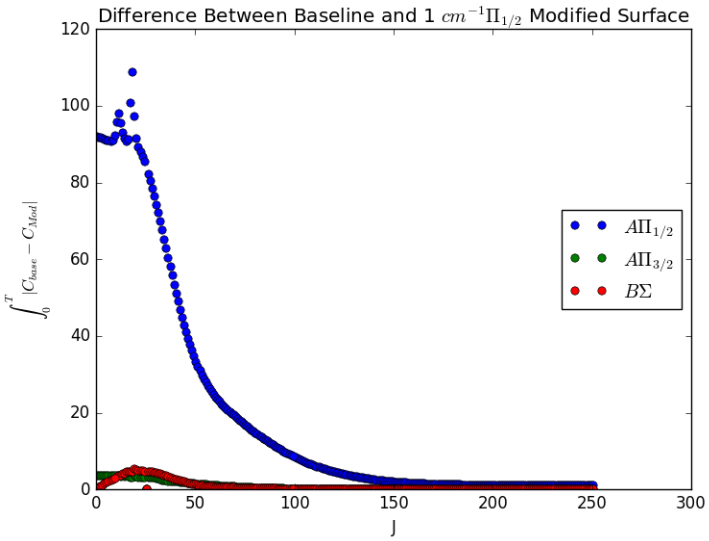

Figure 20. The difference between the baseline correlation and the $1cm^{-1}$ modification falls off as J increases and the angular potential dominates.

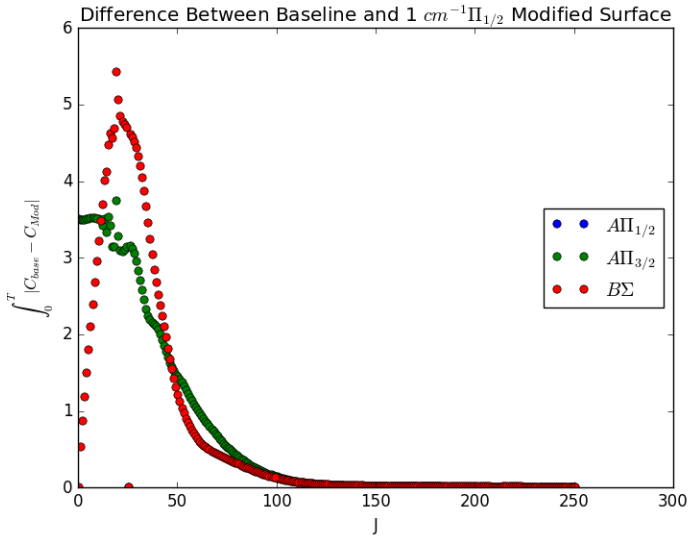

Figure 21. The $\Pi_{3/2}$ and $\Sigma_{1/2}$ demonstrate the same fall off with the Coriolis potential that the $\Pi_{1/2}$ under goes, but with a much smaller magnitude.

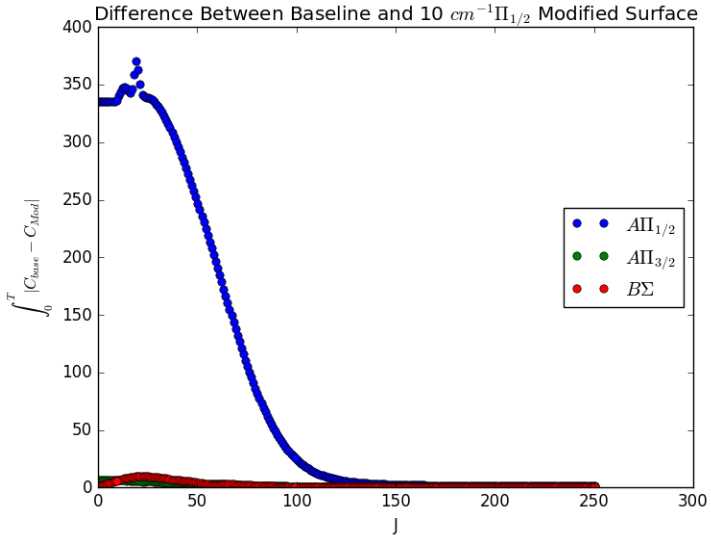

Figure 22. The difference between the baseline correlation and the $10cm^{-1}$ modification falls off as J increases and the angular potential dominates.

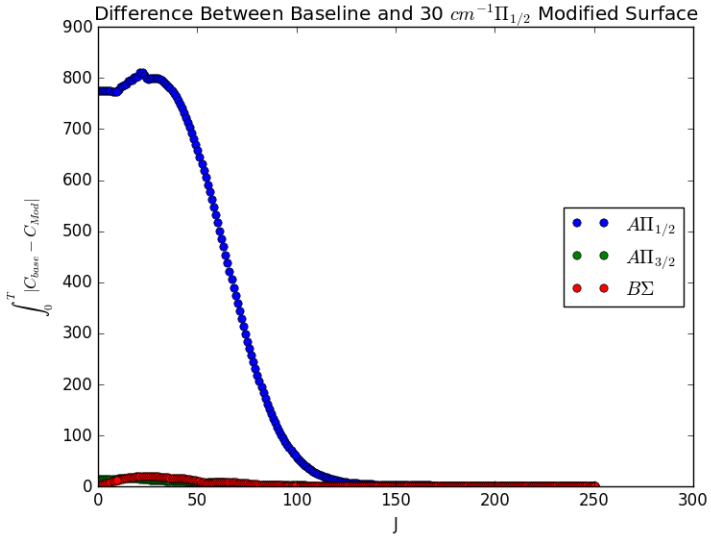

Figure 23. The difference between the baseline correlation and the $30cm^{-1}$ modification falls off as J increases and the angular potential dominates.

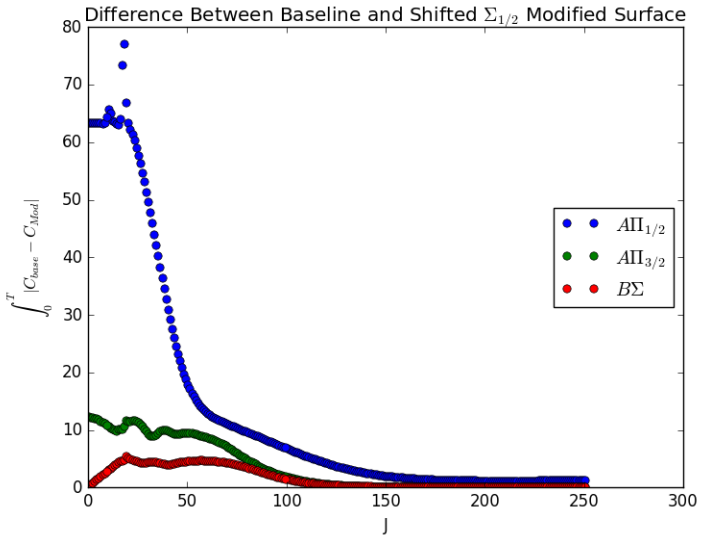

Figure 24. The difference between the baseline correlation and the $\Sigma_{1/2}$ modification falls off as J increases and the angular potential dominates.

A peak occurs in the correlation analysis for $J = 16.5-22.5$. Why this peak occurs is uncertain but speculation points it being the point where the centripetal potential and electronic potential are nearly equal. This is supported by Figs 25 and 26 which shows the difference between correlation functions of the baseline and $10cm^{-1}$ surface for select values of J. The oscillations for J=22.5 and J=23.5 are sharper and more frequent than the rest of the J values. It is possible that these mid range J values are creating a resonance between the angular momentum surface and the electronic potential.

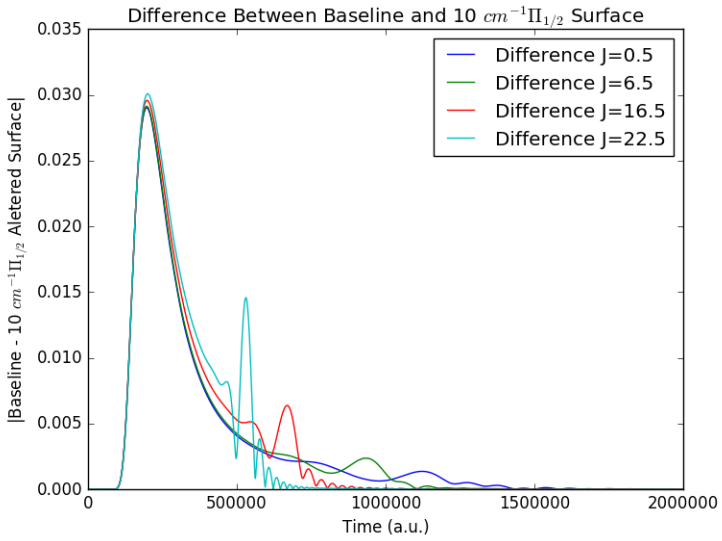

Figure 25. Differences in the correlation function for select J's show oscillations of different magnitude and duration. These oscillation increase in magnitude as J increases. This peak is caused by the low energy portion of the wave packet spending less time interacting with the potential due to the increased barrier.

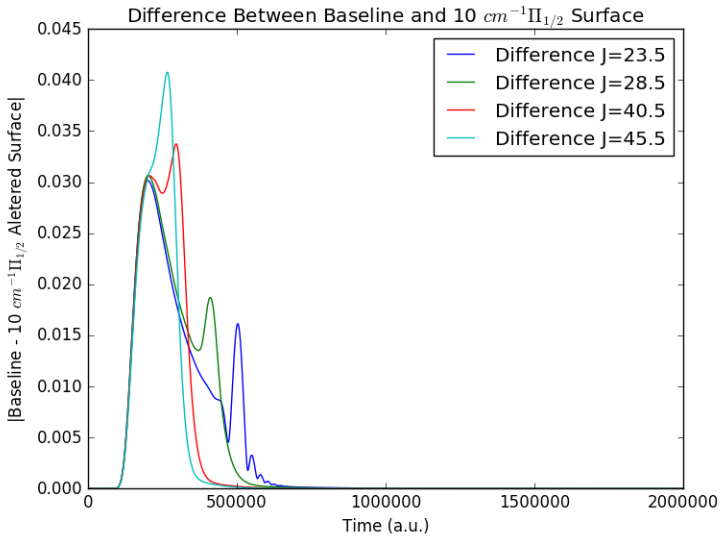

Figure 26. As J increases beyond J=23.5 the oscillations change into one peak as it merges into the bulk of the correlation function. There are fewer oscillations as the angular momentum potential begins to dominate the electronic potential leading to more of the wave packet being reflected.

5.2 S-matrix Analysis

The correlation function analysis gives an idea of what is happening in the time domain. The S-matrix elements give information on how the changes in the surfaces effect the wave packet in the energy domain. Fig 27 shows that the S-matrix elements of the 1 cm^{-1} altered surface at J=0.5 behave very similarly to the baseline.

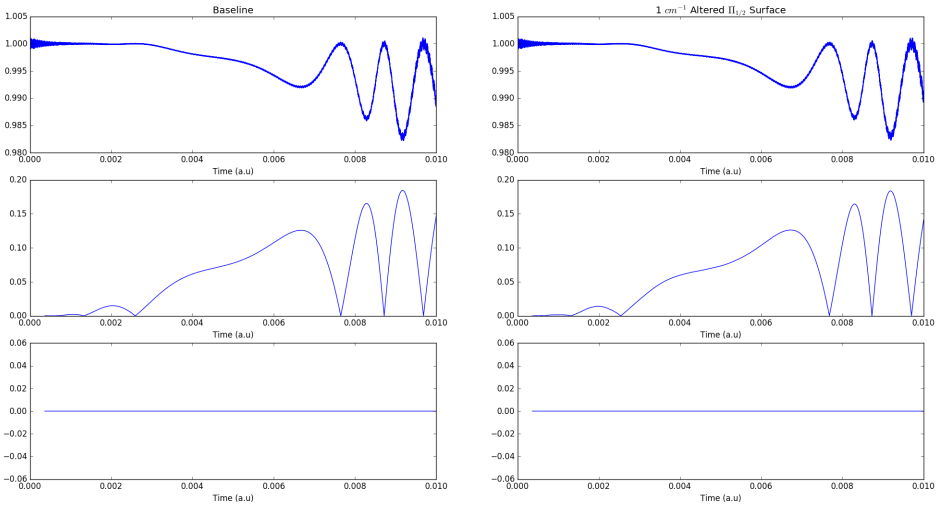

Figure 27. S-matrix elements at J=0.5 for both the baseline and 1 cm^{-1} surface are plotted against each other, with the top plots being the $\Pi_{1/2}$ to $\Pi_{1/2}$ reflection, then working down the $\Pi_{1/2}$ to $\Pi_{3/2}$ transmission, and finally the $\Pi_{1/2}$ to $\Sigma_{1/2}$ transmission.

The changes in the J=0.5, 30 cm^{-1} altered surface and the shifted Σ S-matrix elements showed deviations from the baseline but the changes are more subdued than the changes in the corresponding correlation functions. Fig 28 shows an overall greater transmission to the $\Pi_{3/2}$ state, however, the transmission of the lower energy portion of the wave packet is lower.

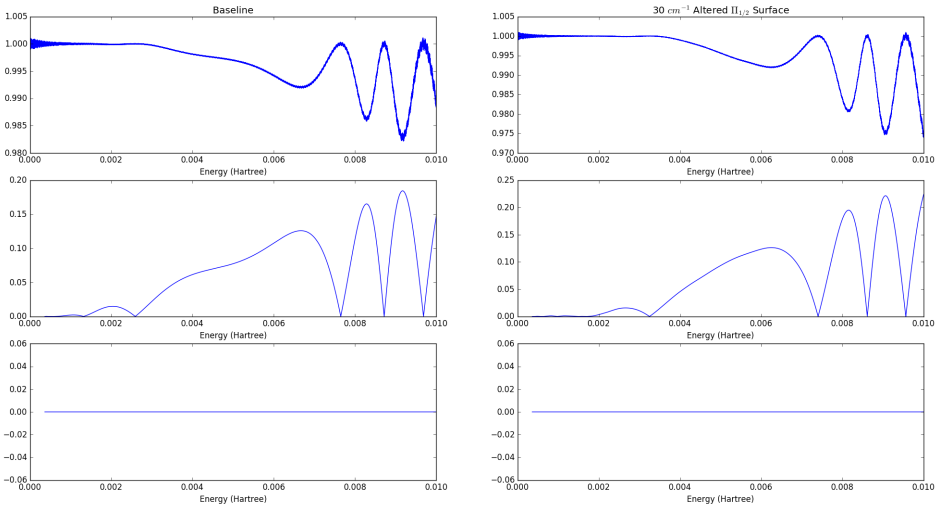

Figure 28. S-matrix elements at J=0.5 for both the baseline and 30 cm^{-1} altered surface are plotted against each other, with the top plots being the $\Pi_{1/2}$ to $\Pi_{1/2}$ reflection, then working down the $\Pi_{1/2}$ to $\Pi_{3/2}$ transmission, and finally the $\Pi_{1/2}$ to $\Sigma_{1/2}$ transmission.

The S-matrix elements for the J=0.5 shifted Σ surfaces in Fig 29 show that transmission to the $\Pi_{3/2}$ surface is lower across the entire energy spectrum with the largest decrease happening around E=0.006 Hartree.

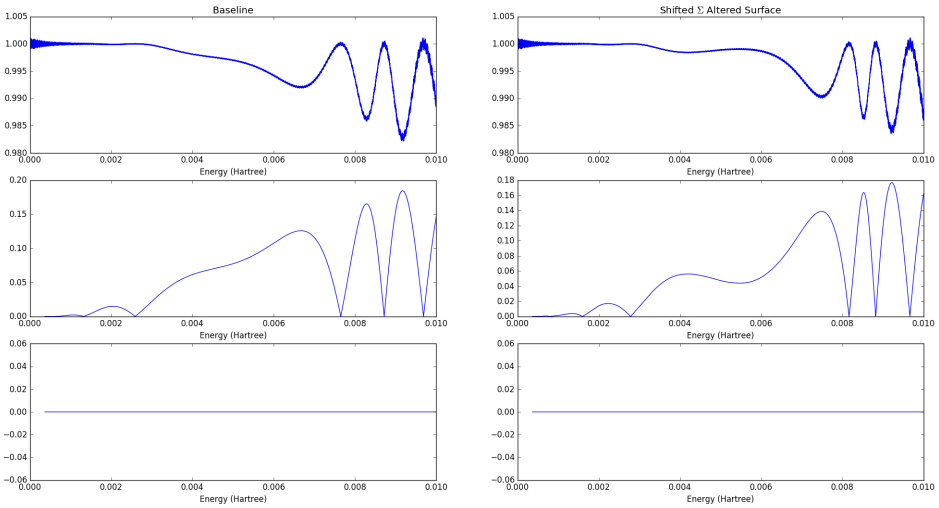

Figure 29. S-matrix elements at J=0.5 for both the baseline and shifted Σ surface are plotted against each other, with the top plots being the $\Pi_{1/2}$ to $\Pi_{1/2}$ reflection, then working down the $\Pi_{1/2}$ to $\Pi_{3/2}$ transmission, and finally the $\Pi_{1/2}$ to $\Sigma_{1/2}$ transmission.

For J=25.5 coupling to the $\Sigma_{1/2}$ state becomes possible. The 1 cm^{-1} changes to the $\Pi_{1/2}$ surface caused no large changes in the behavior of S-matrix elements. For the 30 cm^{-1}, shown in Fig 30, transmission to the $\Pi_{3/2}$ state was dramatically increased for energies above 0.004 Hartree while transmission to the $\Sigma_{1/2}$ was increased for low energies. By increasing the barrier height the energy needed to reach the upper states is decreased making it easier to transmit to the upper states.

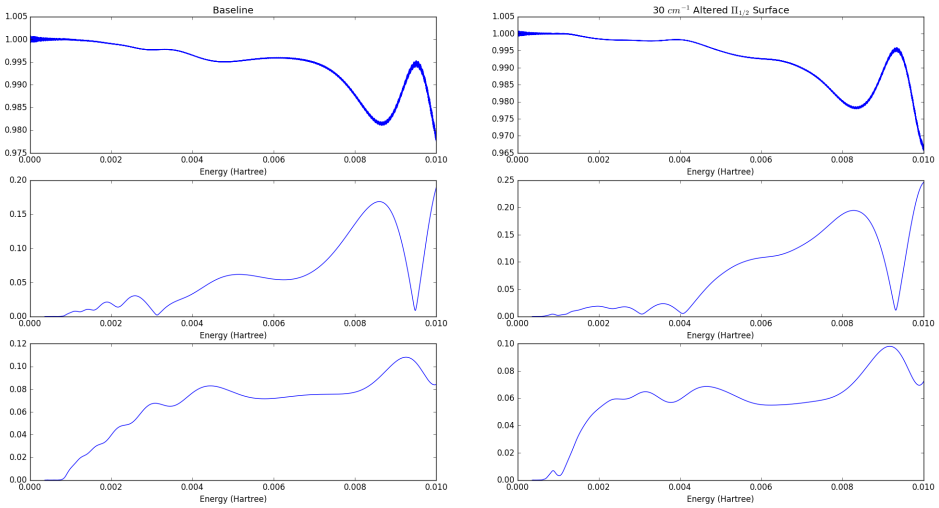

Figure 30. S-matrix elements at J=25.5 for both the baseline and 30 cm^{-1} altered surface are plotted against each other, with the top plots being the $\Pi_{1/2}$ to $\Pi_{1/2}$ reflection, then working down the $\Pi_{1/2}$ to $\Pi_{3/2}$ transmission, and finally the $\Pi_{1/2}$ to $\Sigma_{1/2}$ transmission.

An analysis similar to the correlation function was done by using 32 to find the total difference between the baseline S-matrix elements and the modified surface elements as a function of J.

$$\Delta = \int_0^{E_{max}} |S_{baseline}(E) - S_{Mod}(E)| dE \tag{32}$$

Comparing the differences between the baseline S-matrix and the modified surfaces show, in Figs 31, 32, 33, 34, that there is a fall in the difference as J increases, which is expected. There is also a peak around difference around J=40 in all four figures.

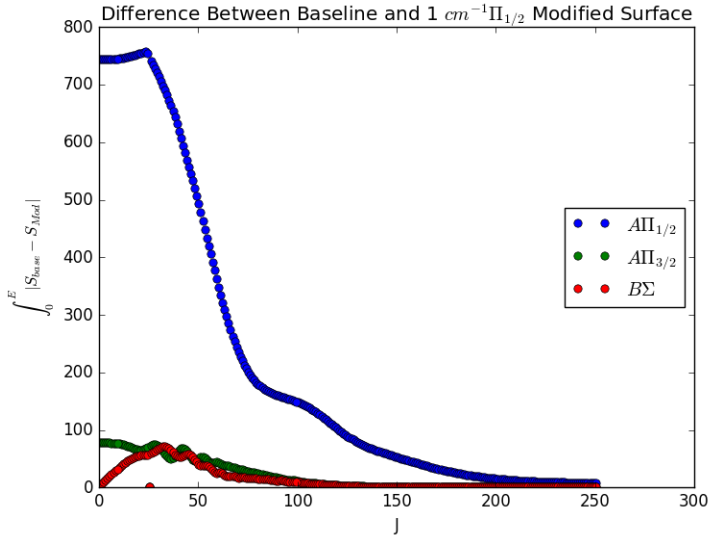

Figure 31. The difference between the baseline S-matrix elements and the $1cm^{-1}$ modification falls off as J increases and the angular potential dominates.

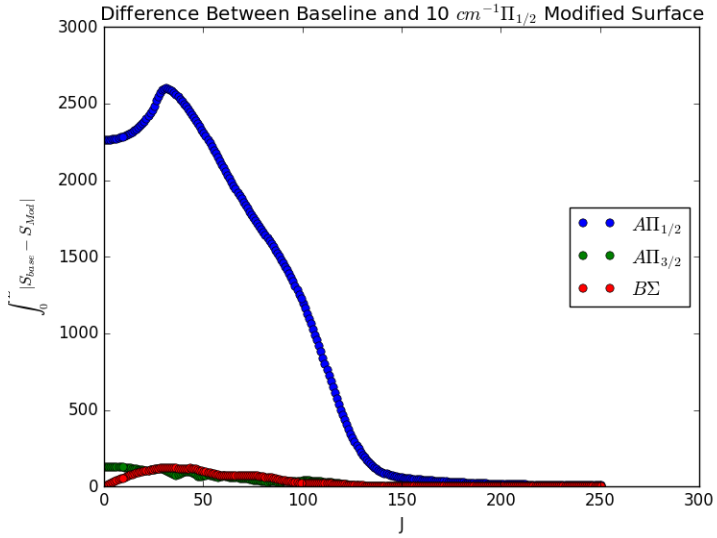

Figure 32. The difference between the baseline S-matrix elements and the $10cm^{-1}$ modification falls off as J increases and the angular potential dominates.

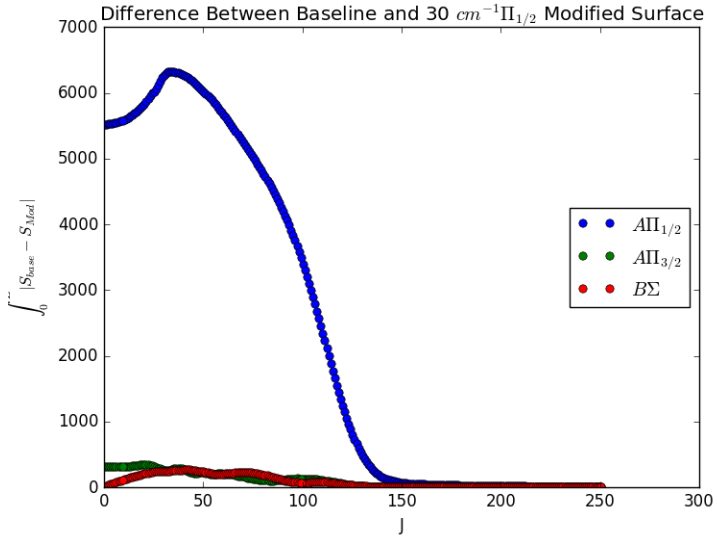

Figure 33. The difference between the baseline S-matrix elements and the $30cm^{-1}$ modification falls off as J increases and the angular potential dominates.

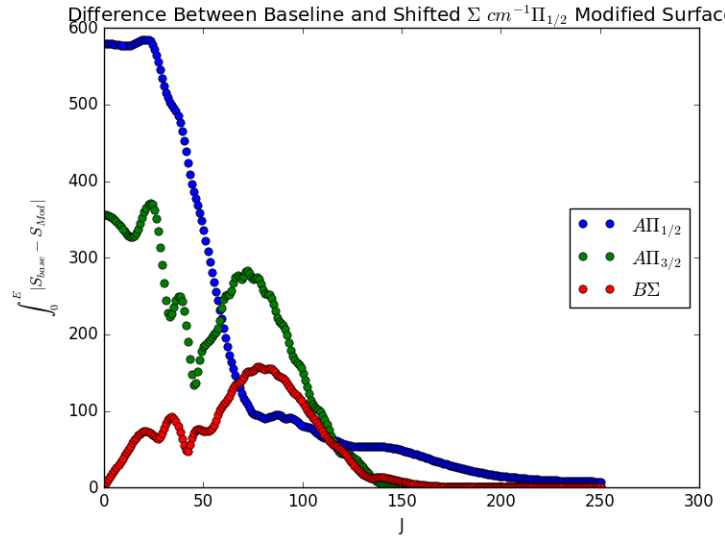

Figure 34. The difference between the baseline S-matrix elements and the shifted Σ modification falls off as J increases and the angular potential dominates.

5.3 Cross Section

In addition to providing transmission and reflection information, S-matrix elements can be used to calculate a theoretical cross section for particle interaction as a function of energy. Eqn. 22 describes the theoretic cross section for state to state interactions. The modified surfaces had a large impact on the theoretic cross section, Fig 35 shows how they deviated from the baseline. The 1 wavenumber surface followed the baseline very closely but the 10 and 30 wavenumber surfaces had a much larger deviation, while keeping the shape of the baseline. Changes to the $\Sigma_{1/2}$ surface caused the largest change in theoretic cross section. The alteration caused large changes in the shape of the cross section.

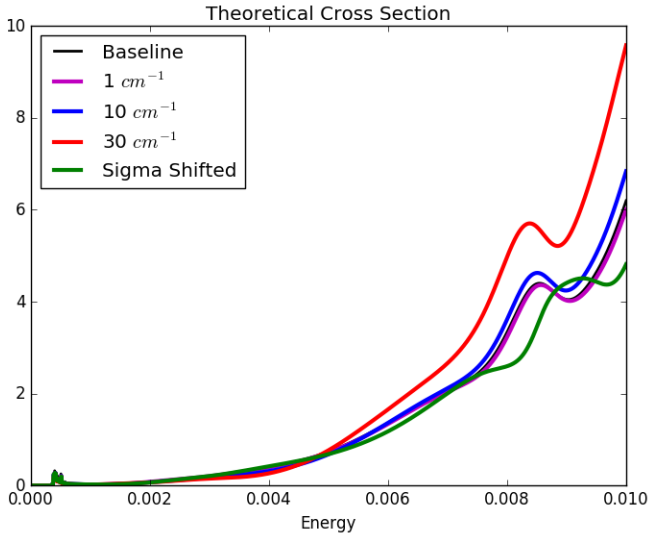

Figure 35. Theoretic cross sections show that modifications to the $\Pi_{1/2}$ surface caused the cross sections to change in magnitude but still follow the same trend. The alterations to the $\Sigma_{1/2}$ surface changed the overall behavior of the cross sections.

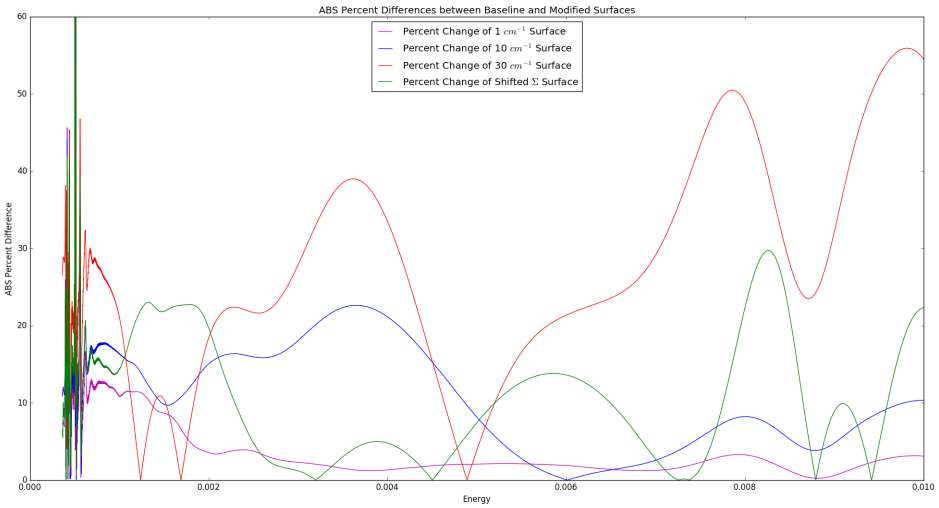

Figure 36. Modifying the surfaces caused large deviations from the baseline calculation in the Shifted Σ and 30 cm^{-1} surfaces. The 1 and 10 cm^{-1} both fall under 10% for higher energies.

This theoretic cross section can then be convolved with the Boltzman distribution to create a thermally averaged cross section using Eqn 24. Fig 37 shows the temperature averaged cross sections for the baseline and all modified surfaces. All cross sections follow the same trend and are closely bunched for all T, meaning that the large changes in the theoretic cross section had little effect on the temperature averaged cross section. The thermal cross section is compared to experimental results in Fig 38. The error bars plotted at 340 and 373 K [12] are from experimental data where the error in the measurements was 10%. All modified surfaces fell within this 10% range at the experimental temperatures.

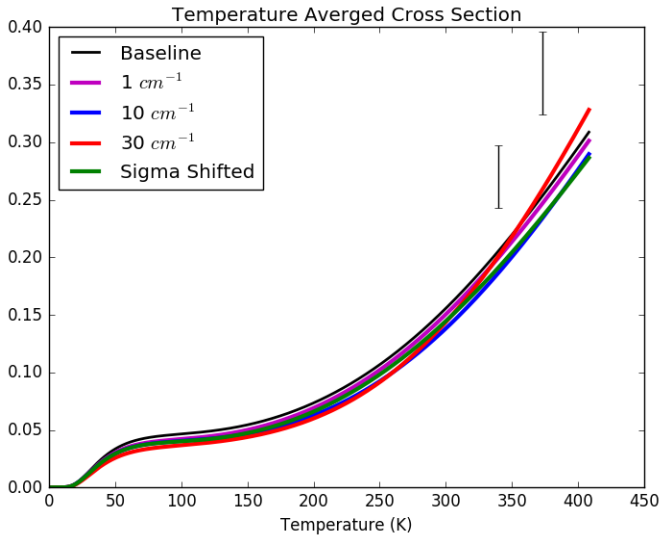

Figure 37. The temperature averaged cross sections all follow the same trend as the baseline and are close in value, despite the large variations in theoretic cross section. The experimental data is from Gallagher [12]

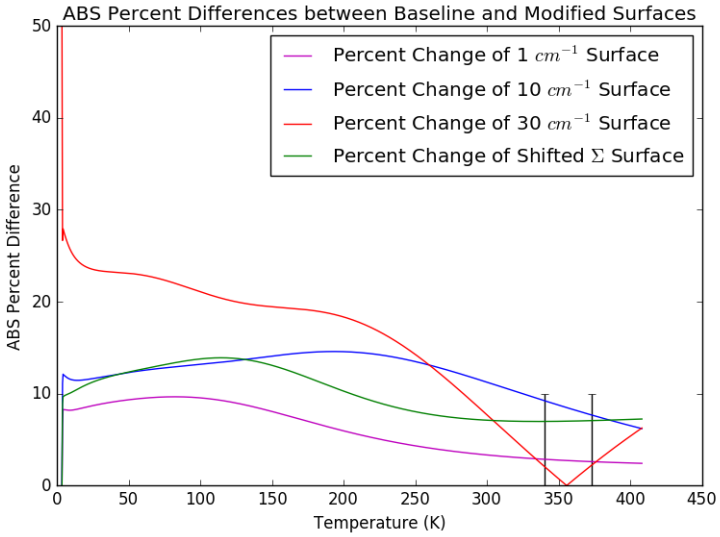

Figure 38. The difference between the baseline and modified surfaces are plotted as a percentage vs temperature. While for low T the error can rise above 10%, for temperatures in the experimental data range the error from the baseline is within the error in experimental measurements, shown by vertical error bars.

VI. Future Work

6.1 Baranger Theory

Semi-classical line broadening and shifting coefficients are calculated using the Anderson-Talman model. This model uses classical collisions of a single atom with an ensemble of particles. These collisions are responsible for the emission of spectral lines that are observed in experiment. The Anderson-Talman model falls short, in that, it calculates broadening and shifting coefficients for each surface independently. This method ignores coupling that exists between states and leads to large errors when compared to the experimental values. The Baranger model uses S-matrix elements to calculate the broadening and shifting coefficients and thus accounts for the coupling between states. [18, 2]

Baranger uses the phase difference in the S-matrix elements to calculate the line broadening and shifting coefficients. The phase for each level is calculated by comparing the imaginary part to the real part of the S-matrix element that corresponds to ground state and the excited state, i.e. the S_{11} and S_{22} elements respectively, as shown in equation (33). The phase difference is the calculated in equation (34).[18] Because ϕ is dependent on energy so is the resulting difference Θ_J, which is calculated for each combination of the total angular momentum, J, and energy, E. The energy is quantized by the initial selection of the spacing of the momentum grid such that $E_{max} = \frac{k^2_{max}}{2\mu}$ and the total angular momentum is quantized by integer increases staring from $J = 0.5$ to $J = 450.5$. The selection of the maximum J value was chosen by comparing what amount of kinetic energy was needed to penetrate into the coupling region to the Coriolis potential.

$$\phi = tan^{-1}(\frac{Im(S)}{Re(S)}) \tag{33}$$

$$\Theta_J(E) = \phi_{excited} - \phi_{ground} \tag{34}$$

Semi-classical broadening and shifting is calculated by integrating over an impact parameter perturbation. The integral over the perturbation parameter in the quantum mechanical system results in the S-matrix elements, as $1 - S_{22}^{-1}S_{11}$, averaged over incident angle. Euler's Rule is the used to rewrite $S_{22}^{-1}S_{11}$ as a magnitude and angle, $exp[i\theta]$. Assuming a Boltzman distribution and quantifying the impact parameter by total angular momentum results in equations (35) and (36) for the broadening and shifting coefficients, in MHz/Torr.

$$\frac{n\alpha}{P} = \sqrt{\frac{2\pi}{\mu^3}}\hbar^2(k_BT)^{-5/2}\sum_{E=0}^{\infty} exp(-\frac{E}{k_BT}\Delta E)\sum_{J=0.5}^{\infty}(2J+1)(1-cos\Theta_J(E)) \tag{35}$$

$$\frac{n\beta}{P} = \sqrt{\frac{2\pi}{\mu^3}}\hbar^2(k_BT)^{-5/2}\sum_{E=0}^{\infty} exp(-\frac{E}{k_BT}\Delta E)\sum_{J=0.5}^{\infty}(2J+1)(sin\Theta_J(E)) \tag{36}$$

VII. Conclusions

This study has shown that temperature averaged cross sections are relatively insensitive to small changes in the electronic potential. With errors within that of experimental results for RbHe, the comparison of the modified surfaces to the baseline shows that a large precision in electronic surface calculations are not needed for cross section calculations and it is not necessary to create high fidelity surfaces as any changes would not be distinguishable from errors in the experimental measurements. There may be other applications, such as line shifting and broadening calculated by the Baranger model, that may be more sensitive due to a change in phase. While the Baranger model does take into consideration the phase of the S-matrix elements it is also convolved with the Boltzman distribution, which was shown to drown out the discrepancies in the theoretic cross section and provide thermally averaged cross sections with a small error. This leads us to believe that any change in the Baranger calculations would be limited.

Bibliography

[1] Alexander, Millard H., Tadeusz Orlikowski, and John E. Straub. "Theoretical study of intramultiplet transitions in collisions of atoms in ^3P electronic states with structureless targets: Ca(^3P)+He". *Physical Review A*, 28(1):73–82, 1983.

[2] Allard, Nicole and John Kielkopf. "The effect of neutral nonresonant collisions on atomic spectral lines". *Reviews of Modern Physics*, 54(4):1103–1118, 1982.

[3] Beach, Raymond J., William F. Krupke, V. Keith Kanz, Stephen A. Payne, Mark A. Dubinskii, and Larry D. Merkle. "Resonance transition 795-nm rubidium laser". *Optics Letters*, 28(23):2336–2338, 2003.

[4] Beahn, T. J., W. J. Condell, and H. I. Mandelberg. "Excitation-Transfer Collisions between Rubidium and Helium Atoms". *Physical Review*, 141(1):83–87, 1966.

[5] Blank, L, D. E. Weeks, and G. S. Kedziora. "M+Ng Potential Energy Surfaces: M = K, Rb, and Cs and Ng = He, Ne, Ar". *in preparation*, 2011.

[6] Boggy, R. and F. A. Franz. "Cross section for $J, m_j \rightarrow J', m_{j'}$ transitions within the 4^2P states of potassium induced collisions with He, Ne, and Kr". *Physical Review A*, 25(4):1887–1899, 1982.

[7] C. D. Lewis, D. E. Weeks. "Theoretical Cross Section of the Inelastic Fine Structure Transition M+Ng ¡-¿ M+Ng for M = K, Rb, Cs, and Ng = He, Ne, Ar". *Journal of Physical Chemistry (under peer review).*

[8] Ciurylo, J. and L. Krause. "$4^2P_{1/2} \leftrightarrow 4^2P_{3/2}$ Mixing in potassium induced in collisions with noble gas atoms". *J. Quant. Spectrosc. Radiat. Transfer*, 28(6):457–461, 1982.

[9] D. E. Weeks, D. J. Tannor. "A time-dependent formulation of the scattering matrix for the collinear Reaction H + H2 (n) ¡ –¿ H2 (n') + H". *Chemical Physics Letters*, 224:451–458, 1994.

[10] D. E. Weeks, R. S. Calfas. "A New Application of Absorbing Boundary Conditions for Computing Collinear Quantum Reactive Scattering Matrix Elements". *Chemical Physics Letters*, 263:292–296, 1996.

[11] Ehrenreich, T., B. Zhdanov, T. Takekoshi, S.P. Phipps, and R.J. Knize. "Diode pumped caesium laser". *Electronics Letters*, 41(7), 2005.

[12] Gallagher, Alan. "Rubidium and Cesium Excitation Transfer in Nearly Adiabatic Collision with Inert Gases". *Physical Review*, 172(1):88–96, 1968.

[13] Griffiths, David J. *Introduction to Quantum Mechanics Second Edition*. Pearson Prentice Hall, Upper Saddle River, NJ, 2005.

[14] Jeffrey I. Steinfeld, William L. Hase, Joseph S. Francisco. *Chemical Kinetics and Dynamics, 2nd Edition*. Pearson Prentice Hall, Upper Saddle River, NJ, 1999.

[15] Jordan, J. A. and P. A. Franken. "Collision-Induced Mixing in the First Excited States of Sodium and Potassium". *Physical Review*, 142(1):20–25, 1965.

[16] Krause, L. "Collisional Excitation Transfer Between the $^2P_{1/2}$ and $^2P_{3/2}$ Levels in Alkali Atoms". *Applied Optics*, 5(9):1375–1382, 1966.

[17] Krupke, William F., Raymond J. Beach, V. Keith Kanz, and Stephen A. Payne. "Resonance transition 795-nm rubidium laser". *Optics Letters*, 28(23):2336–2338, 2003.

[18] Loper, Robert D. *Collisional Broadening and Shift of D1 and D2 Spectral Lines in Atomic Alkali Vapor - Noble Gas Systems*. Ph.D. thesis, Air Force Institute of Technology, 2013.

[19] M. J. McLachlan, D. E. Weeks. "A New Application of the Interaction Picture to Calculate Reactive Scattering Matrix Elements". *Journal of Chemical Physics A*, 102:9489–9493, 1998.

[20] Mies, F. H. "Molecular Theory of Atomic Collisions: Fine-Structure Transitions". *Physical Review A*, 7(3):942–957, 1972.

[21] Nikitin, E. E. "Nonadiabatic Transitions between Fine-Structure Components of Alkali Atoms upon Collision with Intert-Gas Atoms". *J. Chem. Phys*, 43(2):744–749, 1964.

[22] S.H. Yang, T. A. Niday, D. E. Weeks. "Scattering Matrix Elements for the Reaction B ($^2P_{1/2}$) + H_2 (j = 0) $\leftrightarrow$ B($^2P_{3/2}$) + H_2 (j = 0, 2, 4, 6)". *Journal of Chemical Physics*, 125:164301–164315, 2006.

[23] Sharma, A., N.D. Bhaskar, Y.Q. Lu, and W. Happer. "Continuous-wave mirrorless lasing in optically pumped atomic Cs and Rb vapors". *Appl. Phys. Lett.*, 39(3):209–211, 1981.

[24] T., Zhdanov B.V.; Maes C.; Ehrenreich T.; Havko A.; Koval N.; Meeker. "Optically Pumped Potassium Laser". *Optical Communications*, 270, 2007.

[25] T. A. Niday, D. E. Weeks. "Scattering Matrix Elements for the Fine Structure Transition B (2P1/2) + H2 (j = 0) B ¡ –¿ (2P3/2) + H2 (j = 0)". *Chemical Physics Letters*, 308:106–114, 1999.

[26] Tannor, David J. and David E. Weeks. "Wave packet correlation function formulation of scattering theory: The quantum analog of classical S-matrix theory". *J. Chem. Phys.*, 98(5):3884–3893, 1992.

[27] Weeks, David E. and David J. Tannor. "A time-dependent formulation of the scattering matrix using Moller operators". *Chemical Physics Letters*, 207(4):301–308, 1993.

[28] Zweiback, J. and W. F. Krupke. "28W average power hydrocarbon-free rubidium diode pumped alkali laser". *Optics Express*, 18(2):1444–1449, 2010.

REPORT DOCUMENTATION PAGE

Form Approved
OMB No. 0704-0188

PLEASE DO NOT RETURN YOUR FORM TO THE ABOVE ADDRESS.

1. REPORT DATE *(DD-MM-YYYY)*	2. REPORT TYPE	3. DATES COVERED *(From - To)*
23-03-2017	Master's Thesis	September 2016- March 2017

4. TITLE AND SUBTITLE

RbHe Potential Energy Surface Sensitivity Study

5a. CONTRACT NUMBER

5b. GRANT NUMBER

5c. PROGRAM ELEMENT NUMBER

6. AUTHOR(S)

Thorp, Ethan D, 1Lt

5d. PROJECT NUMBER

5e. TASK NUMBER

5f. WORK UNIT NUMBER

7. PERFORMING ORGANIZATION NAME(S) AND ADDRESS(ES)

Air Force Institute of Technology
Graduate School of Engineering and Management (AFIT/EN)
2950 Hobson Way
Wright-Patterson AFB OH 45433-7765

8. PERFORMING ORGANIZATION REPORT NUMBER

AFIT-ENP-MS-17-M107

9. SPONSORING/MONITORING AGENCY NAME(S) AND ADDRESS(ES)

Missile Defense Agency
5700 18th Street, Bldg 245
Fort Belvoir, VA 22060-5573
mda.info@mda.mil

10. SPONSOR/MONITOR'S ACRONYM(S)

MDA

11. SPONSOR/MONITOR'S REPORT NUMBER(S)

12. DISTRIBUTION/AVAILABILITY STATEMENT

Distribution Statement A. Approved for Public Release;Distribution Unlimited"

13. SUPPLEMENTARY NOTES

This work is declared a work of the U.S. Government and is not subject to copyright protection in the United States.

14. ABSTRACT

This paper studies how alterations of features of RbHe potential energy surfaces (PES) for a diode pumped alkali laser (DPAL) system effect the collisional cross section. The Split-Operator method is used to propagate a wave function along these PES and because they are radially coupled, the wave function can be transmitted from the starting surface to other energy surfaces. This transmittance is encoded in the correlation function. The full Hamiltonian used for propagation consists of the electronic potential, the nuclear kinetic energy, and the Coriolis coupling. The correlation function is used to generate the Scattering Matrix elements. These elements describe the transmittance and reflectance coefficients of the reactant wave packet. A temperature averaged cross section is then calculate for the Pi 1/2 to Pi 3/2 transition. Despite large changes in the correlation function and S-Matrix elements, the temperature averaged cross section varied little with change in PES and fell within experimental error margins.

15. SUBJECT TERMS

Diode Pumped Alkali Laser; Potential Energy Surfaces; Rubidium-Helium

16. SECURITY CLASSIFICATION OF:			17. LIMITATION OF ABSTRACT	18. NUMBER OF PAGES	19a. NAME OF RESPONSIBLE PERSON
a. REPORT	b. ABSTRACT	c. THIS PAGE			Charlton David Lewis, II
U	U	U	UU	62	19b. TELEPHONE NUMBER *(Include area code)* 937-255-3636x4695; charlton.lewis@afit.edu

Reset

INSTRUCTIONS FOR COMPLETING SF 298

1. REPORT DATE. Full publication date, including day, month, if available. Must cite at least the year and be Year 2000 compliant, e.g. 30-06-1998; xx-06-1998; xx-xx-1998.

2. REPORT TYPE. State the type of report, such as final, technical, interim, memorandum, master's thesis, progress, quarterly, research, special, group study, etc.

3. DATES COVERED. Indicate the time during which the work was performed and the report was written, e.g., Jun 1997 - Jun 1998; 1-10 Jun 1996; May - Nov 1998; Nov 1998.

4. TITLE. Enter title and subtitle with volume number and part number, if applicable. On classified documents, enter the title classification in parentheses.

5a. CONTRACT NUMBER. Enter all contract numbers as they appear in the report, e.g. F33615-86-C-5169.

5b. GRANT NUMBER. Enter all grant numbers as they appear in the report, e.g. AFOSR-82-1234.

5c. PROGRAM ELEMENT NUMBER. Enter all program element numbers as they appear in the report, e.g. 61101A.

5d. PROJECT NUMBER. Enter all project numbers as they appear in the report, e.g. 1F665702D1257; ILIR.

5e. TASK NUMBER. Enter all task numbers as they appear in the report, e.g. 05; RF0330201; T4112.

5f. WORK UNIT NUMBER. Enter all work unit numbers as they appear in the report, e.g. 001; AFAPL30480105.

6. AUTHOR(S). Enter name(s) of person(s) responsible for writing the report, performing the research, or credited with the content of the report. The form of entry is the last name, first name, middle initial, and additional qualifiers separated by commas, e.g. Smith, Richard, J, Jr.

7. PERFORMING ORGANIZATION NAME(S) AND ADDRESS(ES). Self-explanatory.

8. PERFORMING ORGANIZATION REPORT NUMBER. Enter all unique alphanumeric report numbers assigned by the performing organization, e.g. BRL-1234; AFWL-TR-85-4017-Vol-21-PT-2.

9. SPONSORING/MONITORING AGENCY NAME(S) AND ADDRESS(ES). Enter the name and address of the organization(s) financially responsible for and monitoring the work.

10. SPONSOR/MONITOR'S ACRONYM(S). Enter, if available, e.g. BRL, ARDEC, NADC.

11. SPONSOR/MONITOR'S REPORT NUMBER(S). Enter report number as assigned by the sponsoring/ monitoring agency, if available, e.g. BRL-TR-829; -215.

12. DISTRIBUTION/AVAILABILITY STATEMENT. Use agency-mandated availability statements to indicate the public availability or distribution limitations of the report. If additional limitations/ restrictions or special markings are indicated, follow agency authorization procedures, e.g. RD/FRD, PROPIN, ITAR, etc. Include copyright information.

13. SUPPLEMENTARY NOTES. Enter information not included elsewhere such as: prepared in cooperation with; translation of; report supersedes; old edition number, etc.

14. ABSTRACT. A brief (approximately 200 words) factual summary of the most significant information.

15. SUBJECT TERMS. Key words or phrases identifying major concepts in the report.

16. SECURITY CLASSIFICATION. Enter security classification in accordance with security classification regulations, e.g. U, C, S, etc. If this form contains classified information, stamp classification level on the top and bottom of this page.

17. LIMITATION OF ABSTRACT. This block must be completed to assign a distribution limitation to the abstract. Enter UU (Unclassified Unlimited) or SAR (Same as Report). An entry in this block is necessary if the abstract is to be limited.